Circulation of the European Northwest Shelf: A Lagrangian perspective

Marcel Ricker[1,2*] and Emil V. Stanev[2]

[1]University of Oldenburg, Institute for Chemistry and Biology of the Marine Environment, Carl-von-Ossietzky-Straße 9-11, 26111 Oldenburg, Germany

[2]Institute of Coastal Research, Helmholtz-Zentrum Geesthacht, Max-Planck-Straße 1, 21502 Geesthacht, Germany

*Corresponding author: E-mail: marcel.ricker@uni-oldenburg.de

Abstract

The dynamics of the European Northwest Shelf (ENWS), the surrounding deep ocean, and the continental slope between them are analysed in a framework of numerical simulations using Lagrangian methods. Several sensitivity experiments are carried out in which (1) the tides are switched off, (2) the wind forcing is low-pass filtered, and (3) the wind forcing is switched off. To measure accumulation of neutrally buoyant particles, a quantity named the "normalised cumulative particle density (NCPD)" is introduced. Yearly averages of monthly results in the deep ocean show no permanent particle accumulation areas at the surface. On the shelf, elongated accumulation patterns persist in yearly averages, often occurring along the thermohaline fronts. In contrast, monthly accumulation patterns are highly variable in both regimes. Tides substantially affect the particle dynamics on the shelf and thus the positions of fronts. The contribution of wind variability to particle accumulation in specific regions is comparable to that of tides. The role of vertical velocities in the dynamics of Lagrangian particles is quantified for both the eddy-dominated deep ocean and for the shallow shelf. In the latter area, winds normal to coasts result in upwelling and downwelling illustrating the importance of vertical dynamics in shelf seas. Clear patterns characterising the accumulation of Lagrangian particles are associated with the vertical circulations.

1 Introduction

The European Northwest Shelf (ENWS) (Fig. 1) is among the most studied ocean areas worldwide. Numerous reviews have presented details of its physical oceanography (e.g. Otto et al., 1990; Huthnance, 1991). Understanding the dynamics of the ENWS has been achieved with substantial contributions from Eulerian numerical modelling (Maier-Reimer, 1977; Backhaus, 1979; Heaps, 1980; Davies et al., 1985; Holt and James, 1999; Pohlmann, 2006; Zhang et al., 2016; Pätsch et al., 2017). In contrast, the usefulness of Lagrangian methods for a comprehensive understanding of the ENWS dynamics has not yet been widely investigated heretofore.

In the following, we briefly summarize some basic oceanographic knowledge about the ENWS (the study area is shown in Fig. 1). The slope current dynamics and exchanges between the deep ocean and shelf have been analysed by Huthnance (1995), Davies and Xing (2001), Huthnance et al. (2009) and Marsh et al. (2017); Lagrangian drifter experiments in this area have been described by, e.g. Booth (1988) and Porter et al. (2016). The prevailing westerlies induce on-shelf water transport from the Celtic Sea up to the Outer Hebrides (Huthnance et al., 2009). Water entering the Celtic Sea flows either into the English Channel, into the Irish Sea via St. George's Channel or around the southwest of Ireland (grey arrows in Fig. 1 schematically show the principal shelf circulation). The water exiting the Irish Sea flows around the Outer Hebrides and joins the on-shelf transported water. Part of this water enters the North Sea, mainly via the Fair Isle Current, where it begins an anti-clockwise journey through the North Sea. The third path of waters entering the North Sea originates from the Baltic Sea, subsequently those waters are integrated into a complex system of currents in the Skagerrak and the Norwegian Trench. In this area, the Atlantic and Baltic Sea waters undergo strong mixing. Along the southern slope of the Norwegian Trench, a branch of the European Slope Current flows toward the Baltic Sea, while a current flowing in the opposite direction follows the northern slope of the trench. In addition, large river runoff influences the water masses in the North Sea and along the Scandinavian coast, explaining the low salinity along coastal areas. Further details of the North Sea circulation can be found in, e.g. Howarth (2001) and in the above-mentioned reviews. The major hypothesis in the present study is that

54 although the North Sea is very shallow, it contains an important vertical circulation. Revealing such
55 characteristics is the first specific objective of the present study.
56
57 Much is known about the thermohaline fronts on the ENWS and its estuaries (Simpson and Hunter,
58 1974; Hill et al., 2008; Holt and Umlauf, 2008; Pietrzak et al., 2011). Although large parts of this ocean
59 area are vertically well mixed, seasonal and shorter-term variability lead to pronounced differences in
60 the positions and strengths of the fronts. Freshwater fluxes are also important, particularly in shallow
61 coastal areas. Krause et al. (1986), Le Fèvre (1986), Belkin et al. (2009), Lohmann and Belkin (2014),
62 Mahadevan (2016) and McWilliams (2016) addressed the biological consequences of frontal systems,
63 and the frontal physics are summarized in Simpson and Sharples (2012). However, to the best of the
64 authors' knowledge, the frontal dynamics of the ENWS have not been addressed from a Lagrangian
65 perspective; therefore this will be the second specific objective of our study.
66
67 Most previous studies that employed Lagrangian particle tracking in the region of the ENWS
68 (Backhaus, 1985; Hainbucher et al., 1987; Schönfeld, 1995; Rolinski, 1999; Daewel et al., 2008; Callies
69 et al., 2011; Neumann et al., 2014 and Marsh et al., 2017) addressed only part of the region studied
70 herein. Hence, our overall objective is to provide a comparison among the specific hydrodynamic
71 regimes in different areas of the ENWS and exchanges between these areas. One example has been
72 recently provided by Marsh et al. (2017) for part of the European Slope Current. Lagrangian approaches
73 applied to other ocean regions can be found in, e.g. Bower et al. (2009) for the North Atlantic, Paparella
74 et al. (1997) for the Antarctic Circumpolar Current, Reisser et al. (2013) for Australia, van Sebille et al.
75 (2015) for the world ocean, Maximenko et al. (2018) for tsunamis, Froyland et al. (2014) and van der
76 Molen et al. (2018) in terms of connectivity studies.
77
78 The present study was initiated in the framework of a project studying the fate of marine litter in
79 the North Sea (Gutow et al, 2018; Stanev et al, 2019). Here, we extend the area of our analyses to
80 include the entire ENWS, the European Slope Current, the Bay of Biscay and parts of the Northeast
81 Atlantic. Unlike our recent studies, herein, we address virtual Lagrangian particles ("particles" in the

following) and not real drifters. These particles are transported only by 3-D ocean currents (turbulence, Stokes drift and wind drag are not considered). Thus, this study aims at giving a Lagrangian representation of the velocity field of the ENWS and the surrounding deep ocean.

In Sect. 2, we will describe the model, its setup and the Lagrangian experiments. In Sect. 3.1 and 3.2, Eulerian model results and model validations are presented followed by Lagrangian model results and sensitivity experiments being discussed in Sect. 4.1 to 4.5. The paper ends with a brief conclusion in Sect. 5.

2 Materials and methods

2.1 The numerical model

The Nucleus for European Modelling of the Ocean (NEMO) hydrodynamic ocean model is used in this paper (Madec, 2008). For this study, the Atlantic Margin Model configuration with a 7 km resolution (AMM7; Fig. 1) of NEMO is chosen because it appears to be one of the best validated model setups for the ENWS (O'Dea et al., 2012 and 2017). The numerical model solves the primitive equations using hydrostatic and Boussinesq approximations. The horizontal resolution is $^1/_9°$ in the zonal direction and $^1/_{15}°$ in the meridional direction; that is, the resolution is approximately 7.4 km. This lateral resolution allows for resolving, e.g. tidal mixing fronts, modification of tidal ellipses by stratification, strong shear stresses induced by tides, and eddies with diameter larger than 30-40 km. Not fully resolved are, e.g. frontal jets and shelf break downwelling (Stanev and Ricker, 2020). There are 297 × 375 grid points altogether and 51 vertical σ-layers. For tracer, i.e. temperature and salinity, advection, we employ the total variation diminishing (TVD) scheme, diffusion takes place on geopotential levels with a Laplacian operator (the constant horizontal eddy diffusivity is specified as 50 $m^2\ s^{-1}$). For momentum diffusion, a bi-Laplacian scheme is applied to act on the model levels (constant coefficient of = $-1 \cdot 10^{10}\ m^4\ s^{-1}$). The generic length scale (GLS) k-ε scheme is used as the turbulence closure scheme; the bottom friction is nonlinear with a log-layer structure, a roughness length of $3 \cdot 10^{-3}$ m and a drag coefficient range of $1 \cdot 10^{-3}$ to $3 \cdot 10^{-3}$. The baroclinic time step is 300 s. The output, including the salinity (S), temperature (T), velocities (u, v) and sea surface height (SSH), is written hourly.

The atmospheric forcing is provided by the UK Met Office's atmospheric (NWP) model with a 3-h temporal resolution for the fluxes and an hourly resolution for the 10 m wind and air pressure. The model uses climatological river runoff based on the European HYdrological Predictions for the Environment (E-HYPE) product of the Swedish Meteorological and Hydrological Institute (SMHI). The open boundary forcing has two parts: a tidal harmonic signal (15 constituents, Q1, O1, P1, S1, K1, 2N2, MU2, N2, NU2, M2, L2, T2 ,S2, K2, M4) and the remaining barotropic part consisting of the sea surface elevation and depth-mean currents (2-D surge component). The barotropic forcing was implemented following the Flather radiation scheme (Flather, 1994). In addition to tidal harmonic forcing, tidal potential forcing using the same tidal constituents was applied over the entire model area. The initial and boundary data for temperature and salinity were taken from the operational Forecasting Ocean Assimilation Model (FOAM) AMM7 setup. Further details about the model setup are given in Stanev and Ricker (2020), where the same model configuration has been first used. The period of integration considered here spans from 1 January 2014 to 31 December 2015 of which the first year is the spin-up period. The analyses of the results are performed for the area between 42.57° N–63.50° N and 17.59° W–13.00° E, which is slightly smaller than the model domain to avoid effects due to the open boundaries.

Although part of this study could be performed using the freely available operational FOAM AMM7 data, we run the abovementioned model to (1) perform Lagrangian simulations online , (2) taking into account time scales shorter than days and (3) carry out some additional sensitivity experiments. In contrast to the operational FOAM AMM7 model setup, the data are not assimilated here. In the following, the basic experiment is referred to as the control run (CR). In one sensitivity experiment, the tides are turned off; this experiment is referred to hereafter as the nontidal experiment (NTE). In two other sensitivity experiments, the wind forcing is low-pass filtered with a moving time window of one week (referred to as the filtered-wind experiment, FWE) or completely turned off (the nonwind experiment, NWE). The changes in the model forcing are applied on 1 January 2015.

138 *2.2. Validation data*

139 For validation of SST, data from the Operational Sea Surface Temperature and Ice Analysis (OSTIA)
140 system is used, which provides a gap-free synthesis of several satellite products (Donlon et al., 2012).
141 Velocities have also been validated using 9 passive GPS surface drifters; these drifters provide the most
142 appropriate type of in situ data for validating the model's ability of particle advection. The drifters,
143 which have a bottom-mounted sail to reduce direct wind drag, were designed to reduce the effect of
144 direct wind drag (see Callies et al. (2017) for a technical description of the drifters). The drifters were
145 released in the German Bight during RV *Heincke* cruise HE445, and their position was sent every ~20
146 minutes from May to July 2015. The dataset is freely available (Carrasco and Horstmann, 2015) and to
147 the best of the authors' knowledge, it is the only GPS drifter dataset available for the ENWS during the
148 period of the simulations analysed herein. For validation, the model velocities are interpolated to the
149 drifter positions in space and time. Drifter velocities are also compared with independent observations
150 using HF radar data. The HF radar system described by Stanev et al. (2015) and Baschek et al. (2017)
151 consists of 3 measurement stations covering most of the German Bight and measures ocean surface
152 velocities.
153
154 *2.3 Particle release experiments*

155 Particles are released in the hydrodynamic model, and their propagation is used to analyse the transport
156 properties. The experiments were carried out "online"; that is, the particle trajectories were computed
157 within the hydrodynamic model at every time step. Additional experiments were carried out "offline"
158 using the model velocity output. High-frequency processes and vertical transport are better accounted
159 for in the former experiments, whereas backtracking is only possible offline. An intercomparison
160 between the online and offline integrations using the same particle setup demonstrated that neither
161 approach leads to drastic differences when comparing 2-D horizontal particle transport properties.
162
163 The online advection of particles was achieved by the freely available open-source ARIANE model.
164 The version of ARIANE implemented in NEMO has frequently been used in other studies, e.g. Blanke
165 and Raynaud (1997) and Blanke et al. (1999). Further details of the ARIANE model can be found in

166 the appendix of Blanke and Raynaud (1997) and in the ARIANE user manual (stockage.univ-
167 brest.fr/~grima/Ariane/). Beaching is not possible; that is, the total number of particles remains constant
168 over time. An extra wind drag is not used, nor is additional horizontal and vertical diffusion for the
169 particles (pure Lagrangian particles). Actually, velocity gradients together with a small advection time
170 step (van Sebille et al., 2018) provide a sufficiently high shear diffusion. The vertical velocity is taken
171 into account and the particle positions are written hourly. Particles are neutrally buoyant and provide a
172 Lagrangian representation of the velocity field.
173
174 Different seeding strategies were implemented. In one class of experiments (#1–4 in Table 1), the
175 particles were seeded laterally at 1 m (surface particles), as well as in the grid cells just above the
176 seafloor (bottom particles) over the whole domain. In the second experiment (#5 in Table 1) named CR-
177 B, the particle tracking process was carried out offline. For this purpose, the freely available open-
178 source model OpenDrift (Dagestad et al., 2017) was used, in which the particles were advected by a
179 2nd-order Runge–Kutta scheme. The offline calculation was performed backward in time at a constant
180 depth with a velocity input time step, a model time step and an output time step of 1 h. The particle
181 release depth in this experiment was 1 m. In a third experiment (#6 in Table 1) named CR-V, particles
182 were released in a 100 km wide strip extending oceanward from the 150 m isobath starting in the Bay
183 of Biscay and ending north of the Shetland Islands at 61.7° N (red and blue coloured area in Fig. 9a–
184 d). In this experiment, particles were seeded vertically every 20 m; this is exemplarily shown for the
185 depth 900–1,000 in Fig. 9e.
186
187 The seeding strategy was consistently executed as follows. The initial distribution of particles was
188 uniform with 1 particle per model grid cell, that is, 64,831 particles per depth layer for the whole domain
189 (experiments #1–5 in Table 1) and a total of 345,011 particles in experiment #6. In the CR and CR-V
190 (experiments #1 and 6, respectively), particle release was repeated on the first day of every month in
191 2015, and particles were traced for 1 month. Thus, 12 data sets, each including 1 month of trajectory
192 data, were generated. Additionally, for the seeding in January, the particle positions were traced for 6

months. The FWE, NWE and CR-B (experiments #3–5, respectively) were conducted only for January 2015 whereas the NTE (experiment #2) was run until the end of July 2015.

Experiment #1 aims to understand and visualise the general circulation of the ENWS at both the surface and bottom. The uniform initial distribution of particles enables a comprehensive Lagrangian representation of surface and bottom dynamics over the whole domain. This experiment will also be used to analyse accumulation and dispersal areas as well as vertical dynamics and frontal effects. Further, it serves as the reference run for the sensitivity experiments. The sensitivity experiments (experiments #2–4) are performed to assess the influence on Lagrangian dynamics of some of the most important drivers for particle advection, i.e. tides and wind. Experiment #5 supports the analyses of vertical shelf dynamics and complements experiment #1. Experiment #6 provides a 3-D particle seeding along the continental slope to study the dynamics there.

Table 1: Summary of the particle release experiments; further details are given in Sect. 2.3. Surface release is done at 1 m depth and bottom release one grid cell above the sea floor. Particle release was done once at the beginning of each month.

# (abbr.)	Particle advection		Spatial seeding			Integration time	Details
	Online	Offline	Whole domain	Shelf edge	Vertical		
1 (CR)	x		x		surface & bottom	12 x 1 month	3-D particle motion
2 (NTE)	x		x		surface & bottom	January + July	no tides,3-D
3 (FWE)	x		x		surface & bottom	January	filtered wind, 3-D
4 (NWE)	x		x		surface & bottom	January	no wind, 3-D
5 (CR-B)		x	x		surface	January	backtracking, 2-D
6 (CR-V)	x			x	every 20 m	12 x 1 month	only shelf edge, 3-D

2.4 Normalised cumulative particle density

The analyses of the results will focus on typical Lagrangian properties, e.g. the positions of the particles and their trajectories. Such a presentation could be considered inferior compared with the Eulerian presentation, which displays the concentrations of properties. However, from these Lagrangian characteristics, one can derive properties similar to the concentration that can represent the "compaction" process of particles in certain areas or identify the areas that are more frequently visited

by the particles. These properties related to particle density allow the areas in which particles accumulate to be identified.

Different approaches to quantify particle accumulation have been proposed (Koszalka and LaCasce; 2010; Koszalka et al., 2011; van Sebille et al., 2012; Huntley et al., 2015). Below, in addition to the typical Lagrangian properties, a property named the "normalised cumulative particle density (NCPD)" is introduced that measures the number of particles that have visited each grid cell during a certain time interval. This quantity is normalised by the corresponding number of initial particles in the respective NCPD grid cell for the same time interval (in our case 1 particle per grid cell), which corresponds to a motionless situation:

$$NCPD(x, y, t_n) = \frac{\sum_{i=0}^{n} N_{u\neq 0}(X,Y,t_i)}{\sum_{i=0}^{n} N_{u=0}(X,Y,t_i)} \quad (1)$$

where *NCPD* is the normalised cumulative particle density, (*X*, *Y)* are the coordinates of an arbitrary grid cell in longitudinal and latitudinal direction, respectively, with dimensions (*dX*, *dY*), *n* is the number of time steps from t_0 to t_n, *u* is the velocity field and *N* is the number of particles at time step *i* in grid (*X*, *Y*). In the present study, (*dX*, *dY*) represent the model grid dimensions (*dx*, *dy*), but could be larger or smaller for other applications. A NCPD greater (smaller) than unity corresponds to more (fewer) particles, which are identified in a grid cell on average, than there would be without currents. Thus, the NCPD can be interpreted as the percentage of the initial number of particles averaged over time, or as proportional to the inverse residence time.

The definition of the NCPD is not straightforward if the initial particle concentration is zero in some areas. If the number of particles in some areas remains small (e.g. areas close to an inflow-dominated open boundary or divergence zones), the statistical confidence of this property cannot be ensured. Therefore, areas where the NCPD is less than 30 % are excluded from the analysis (white areas in the following figures). In the present study, the focus will be on monthly time scales (t_n = 1 month). Choices

of (*dX*, *dY*) and of the particle seeding have been made accordingly. For comparison, for integration times longer than one month, large areas remain free of particles; integration times shorter than one month would cause rather noisy results.

3 Eulerian model results

3.1 Analysis of the simulated dynamics

The circulation of the CR is very diverse in different model areas, but the differences among the dynamic regimes in the CR are most pronounced between the deep ocean and the shelf. The residual velocities (U) and velocity amplitudes for January 2015 (Fig. 2a and 2b) show basically two regimes: an eddy-dominated regime west of the continental slope and a tidally dominated regime on the shelf. The latter is characterized by relatively low residual velocities (Fig. 2a) and large velocity oscillations in the English Channel, Southern Bight, Irish Sea and Celtic Sea (Fig. 2b). The transition between these two regimes occurs along the 200 m isobath (Fig. 2a), which can be considered a separation line between the dynamics of the shelf and deep ocean. A sequence of mesoscale eddies is developed offshore of the western shelf edge with a dominant one in the Rockall Trough (Fig. 2a and 2b), which are also readily visible in the corresponding SSH pattern (not shown). The largest amplitudes of the sea level oscillations are observed around the British Isles and along the southern coasts of the German Bight. The dominant wind direction is from the west due to the prevailing westerlies (Fig. S1 in the supplementary material).

The simulated thermohaline characteristics are consistent with the existing knowledge: the coastal waters, particularly those in the German Bight, are less saline (Fig. 2c) and represent typical regions of freshwater influence (ROFIs). In the German Bight, most of the low-salinity water originates from the Rhine, Ems, Weser and Elbe Rivers and spreads along the German and Danish coasts before it reaches the Skagerrak, where it mixes with the low-salinity outflow from the Baltic Sea. The pattern of the salinity gradient (Fig. 2d) reveals features along the coasts and at the major fronts in the German Bight. Additionally, the two current branches in the Norwegian Trench associated with two opposing flows

(one flowing to the east along the southern slope and another flowing in the opposite direction along the northern coast) are also easily observed as areas characterised by large salinity gradients.

In January, the overall temperature distribution is characterized by cold temperatures on the shallow shelf and a south-north temperature gradient in the deep water south of Ireland (Fig. 2e). A warm water plume exits the English Channel (Fig. 2e) and traces the pathway of warm Atlantic water into the North Sea, which is also known from satellite observations (Pietrzak et al., 2011). At the northern boundary of this plume, the East Anglia Plume is known to transport suspended particulate matter (SPM) to the northeast. Along with a second plume extending into the Irish Sea, they are visible as strong temperature gradients (Fig. 2f). The temperature gradient also reveals a number of mesoscale features occurring in the deep ocean along the rims of currents (compare Fig. 2f with 2a). In July, the warmest temperatures can be found in the Bay of Biscay and along the coasts of the shallow shelf, especially on the Armorican Shelf (Fig. S2a). The July temperature distribution is also characterized by well-pronounced temperature gradients, e.g. the Frisian Front located somewhat north of the Dutch coast. The simulated gradients along the Celtic Sea Front, Ushant Front, Islay–Malin Head Front and the Flamborough Head Front (black circles in Fig. S2a) support the results of Pingree and Griffiths (1978). The disappearance of these fronts in the results of the NTE demonstrates that they are tidal mixing fronts (see Fig. S2a and S2b). Overall, Fig. 2a–f support much of what is known from previous studies about the general dynamics and thermohaline characteristics of the ENWS (e.g. Pätsch et al., 2017).

Understanding the differential properties of currents is of utmost importance to understand the propagation of Lagrangian particles. Therefore, we will present a brief analysis of deformation, as proposed by Smagorinsky (1963):

$$|D| = \sqrt{{D_T}^2 + {D_S}^2} = \sqrt{\left(\frac{\partial u}{\partial x} - \frac{\partial v}{\partial y}\right)^2 + \left(\frac{\partial \mathrm{u}}{\partial \mathrm{y}} + \frac{\partial \mathrm{v}}{\partial \mathrm{x}}\right)^2} \quad (2)$$

with horizontal tension strain

$$|D_T| = \sqrt{\left(\frac{\partial u}{\partial x} - \frac{\partial v}{\partial y}\right)^2} \quad (3)$$

and horizontal shearing strain

$$|D_S| = \sqrt{\left(\frac{\partial u}{\partial y} + \frac{\partial v}{\partial x}\right)^2} \quad (4)$$

with (u, v) being the model velocities components and (∂x, ∂y) the model grid size in longitudinal and latitudinal direction, respectively. Figure 2g shows the 24.84-h averaged (two M_2 cycles) deformation obtained from the CR surface currents on 15.01.2015 (the influence of the most dominant tidal constituent is excluded). The order of this property O (10^{-5}) is within the ranges measured by Molinari and Kirwan (1975) with Lagrangian drifters in the Caribbean Sea. The most obvious features are the two large areas on the shelf exhibiting low deformation, namely, the North Sea and the Celtic Sea, including the Armorican Shelf connected by the English Channel and Southern Bight, where several localised high-deformation areas appear (compare Fig. 2g with 2b). High-deformation areas are also present in the Irish Sea extending to the northern coast of Ireland. The difference of deformation between the NTE and CR (i.e. NTE minus CR) can be related to tides and clearly shows their impact on these three areas (Fig. 2h). In addition to shallow, enclosed areas, the deformation along the shelf edge of the Celtic Sea is also affected by tides. High-deformation features in the deep ocean arise at the eddy boundaries (compare Fig. 2g with 2a) and most of them are also present in the NTE. Hence, flow deformation is expected to be of significant importance for water masses in the deep ocean. Exceptions are the Bay of Biscay and the northwest of the domain where the deformation is less pronounced in the NTE. The difference patterns there have scales of mesoscale eddies suggesting that these eddy dynamics could be coupled to the one of tides. In the Norwegian Trench, high deformation is observed along the southern 200 m isobath. Here, the influence of tides arises as small-scale patterns associated with the interaction of the two currents.

323

324 *3.2 Model validation*

325 The root mean square difference of January 2015 SST of the model and OSTIA data reveals values
326 smaller than 1.5°C in vast areas of the model domain, whereas values between 0.5 and 1.0°C are the
327 typical range (Fig. S3).

328

329 Scatter plots of drifter and model velocities show a good model performance in the range of ±25
330 cm s^{-1}, where the quantile-quantile plot (qq-plot) is almost along the diagonal (Fig. S4a and S4b).
331 Deficiencies in the model occur at higher velocities, where the model is too slow probably due to the
332 neglected direct wind drag and Stokes drift (Röhrs et al., 2012; Stanev et al., 2019). Nevertheless, the
333 linear correlations of the u and v velocity components of 0.88 and 0.84, respectively, between the
334 drifters and the model and the corresponding RMSEs of 14.3 and 12.4 cm s^{-1} are considered to reflect
335 a satisfactory model performance (Table 2).

336

337 The quality of the above numbers illustrating the model skill can be better understood if the drifter
338 data are compared with independent observations using HF radar data. The corresponding scatter plots
339 (Fig. S4c and S4d) do not show as much underestimation of high velocities as in the model (compare
340 with Fig. S4a and S4b), but the spread of the data in two observations is comparable to the case of the
341 model-data comparison (the standard deviation between the two observations is even larger than in the
342 case of the model-data comparison). The conclusion from Table 2 is that the difference between the
343 estimations from the model and data are not larger than that between two observations. Similar
344 validations provided by Stanev et al. (2019) for the North Sea also demonstrate the credibility of the
345 Lagrangian tracking approach.

346

347 **Table 2**: Summary of the model velocity validation performed by comparing GPS drifter velocities
348 with the CR and HF radar velocities; the surface velocity components of the latter were interpolated to
349 the drifter velocities. Details are given in the text. A positive bias denotes that drifter velocities are

larger than the velocities of the CR or HF radar. The corresponding scatter plots are given in Fig. S4. n is the number of observations.

	Drifter – CR (n = 10,339)		**Drifter - HF radar** (n = 353)	
	u	v	u	v
RMSE [cm s^{-1}]	14.6	12.5	18.4	12.6
Linear correlation	0.88	0.84	0.91	0.87
Standard deviation [cm s^{-1}]	14.3	12.4	16.9	12.4
Bias [cm s^{-1}]	2.9	1.5	7.4	-2.0

4 Lagrangian model results

4.1 Overall analysis of trajectories and particle dynamics

The particle trajectories (Fig. 3) of the CR (experiment #1, see Table 1) show the well-known, dynamic features of the ENWS and the surrounding deep ocean. In relatively shallow areas, e.g. the English Channel, Southern Bight and Irish Sea, the surface and bottom currents are almost parallel (Fig. 3a and 3b). This is typical for tidally influenced, wind-driven shallow water circulation. Trajectories symbolising currents appear relatively thick in the areas dominated by strong tides because the large-scale presentation cannot effectively resolve small tidal excursions. This is supported by the magnified representation of the dynamics in Fig. 3c and 3d. After 12.42 h, the trajectories on the shelf present as nearly closed circles. The difference between the start and end positions on the circular loops give an estimate of the net transport, which is much smaller than the tidal excursions. The net transport rapidly increases, and the tidal excursions decrease further off-shelf beyond the 900 m isobaths, where the mesoscale dynamics are dominant. As in the case of the Eulerian visualisation of the velocity field, the 200 m isobath can be considered as the boundary separating the dynamics of the shallow and deep ocean. The meandering of the European Slope Current along the shelf edge (at ~500–2,000 m) is pronounced from the Bay of Biscay to the Goban Spur and around the Porcupine Bank (Fig. 3b). The Skagerrak and Norwegian Trench also show pronounced mesoscale dynamics (Fig. 3d).

373 *4.2 Surface and bottom patterns of the particle distribution*

374 Despite some similarities between the surface and bottom trajectories (Fig. 3), the particle accumulation
375 patterns in shallow areas are considerably different (Fig. 4). To investigate these differences, the
376 positions of the particles released in January (CR, experiment #1, see Table 1) are displayed in Fig. 4.
377 After 1 month, the surface-released particles accumulate mainly along narrow patterns on the shelf and
378 in the Skagerrak (Fig. 4a). In contrast, the coastal regions around Great Britain and Ireland (but also in
379 the German Bight) can be considered divergence zones. The particle distribution in the deep ocean also
380 shows small strip-type patterns, especially in the southwestern part of the model domain and will be
381 discussed in detail later (see Sect. 4.3). In the following, examples of pronounced accumulation and
382 dispersal features are given.

383

384 There is a tendency for the bottom-released particles to leave areas with a steep bottom slope. The
385 most obvious example is the continental slope are along the 200 m isobath from the Spanish coast
386 around the Goban Spur and Porcupine Bank (Fig. 4b) until the Norwegian Trench. Van Aken (2001),
387 Huthnance et al. (2009) and Guihou et al. (2018) demonstrated that slope currents, downward flows of
388 shelf water and internal waves, respectively, dominate the dynamics of the ENWS continental slope.
389 These processes can induce a net transport and in turn a tendency of bottom-released particles to leave
390 the continental slope.

391

392 After 6 months, vast areas of the shelf and the western part of the domain become free of particles.
393 The particles flow from the English Channel along the Frisian Front in the south and the Fair Isle
394 Current in the north into the inner North Sea (Fig. 4c). The pattern in the Irish Sea is similar to the
395 Frisian Front: a narrow strip of particles in the middle of this basin is the remnant of a similar strip from
396 an earlier time (Fig. 4a) connecting the source of particles (in the south) to their sink (in the north). The
397 region around the Orkney and Shetland Islands accumulates particles owing to on-shelf transport by the
398 westerlies, which also drives particles away from the western open boundary. This region additionally
399 receives particles from the south originating from the Irish Sea or floated around the western coast of
400 Ireland; in both cases, these particles are sourced from the deep ocean. Likewise, the Bay of Biscay

accumulates particles on time scales of several months. Bottom accumulation on the shelf occurs mainly west and south of the Dogger Bank (Fig. 4d). Also the bottom trajectories (Fig. 3b) show that particles north of Dogger Bank are forced to flow around its western edge through the Silver Pit into the Oyster Ground (see the bathymetry in Fig. 1) suggesting topographically influenced particle motions. Once the particles reach this basin, they can flow out only northward along its thalweg until they reach the northeastern edge of Dogger Bank (compare Fig. 4d with Fig. 1).

In the Skagerrak, the situation is as follows. At the bottom, the Norwegian Trench supplies the Skagerrak with particles from the Atlantic along its southern slope. At the surface, the Skagerrak receives particles from the Fair Isle Current, the German Bight and the Baltic Sea. Particles approaching the Skagerrak can become trapped in its circular and eddy-dominated velocity pattern (Fig. 3d and 2b), which extends from the surface down to the bottom (see also Rodhe, 1987; Gutow et al., 2018). In the Norwegian Trench, the particle distribution has high spatial variability due to the irregular mesoscale dynamics.

4.3 Tendencies of particle accumulation

The instantaneous particle positions are not sufficiently representative of their accumulation and dispersal over long periods and can lead to misinterpretations of their accumulation trends. This becomes evident by comparing the particle positions after 1 month (Fig. 4a and 4b) with the NCPD for the same period (Fig. 5a and 5b). Although the general surface and bottom particle patterns (Fig. 4a and 4b) for January 2015 are comparable to the mean accumulation patterns (Fig. 5a and 5b), some features do not coincide. The monthly NCPDs for all twelve months are shown in Fig. S5 and S6 for the surface- and bottom-released particles, respectively. At the surface, only a few accumulation areas are visible on the annual mean map (red areas in Fig. 5c); these areas are located in the Irish Sea (*1*), English Channel (*2*), Southern Bight (*3*), German Bight (*4*), Skagerrak (*5*), at the Fair Isle Current (*6*) and at the northern coasts of Ireland and Great Britain (*7*). Vast coastal areas have a NCPD smaller than 0.3,

implying offshore propagation. Despite the numbered accumulation areas and coasts prone to particle removal, most of the domain shows neither particle accumulation nor removal (NCPD ≈ 1).

At the bottom, particle accumulation is highly variable in the deep ocean, but the removal of particles from areas with steep topography is evident (Fig. 5d). On the shelf, the tendency of particles to propagate away from coasts is smaller than for surface particles; particles even accumulate, e.g. in the German Bight and along the eastern British coast (discussed in detail in Sect. 4.4). Further, accumulation takes place to the south of Dogger Bank and in the Skagerrak. It is worth noting that the major accumulation pattern at the surface along the Frisian Front (*3*, *4*) has as its counterpart a pattern of removal at the bottom (compare Fig. 5c and Fig. 5d). Additionally, coastward of accumulation area *4*, there is a removal area at the surface; in the same area, the bottom pattern shows a tendency of accumulation. These opposite tendencies in the surface and bottom layers suggest that the vertical circulation is also important in shallow environments. The inflow along the southern slope of the Norwegian Trench appears as increased particle accumulation.

There are some prominent small-scale features (strip-like or filament-like characteristics) in the deep ocean occurring as NCPD maxima and minima (Fig. 5a and S5) as well as particle accumulation and dispersal in the particle distribution (Fig. 4a). These features change their positions depending on mesoscale dynamics. They are reminiscent of the attributes reported by Haller and Yuan (2000), who demonstrated that particles initially located outside eddies accumulate in lines along the boundaries between them. When the averages are computed for a longer period, these filaments tend to disappear (compare Fig. 5a with 5c), which is explained by the fact that the time scales of eddy motions are substantially shorter than the annual scale. This follows from the changes in the position and occurrence of the strip-type areas with NCPDs greater than 1 from month to month (compare the results from single months of Fig. S5). A more profound Lagrangian representation of eddies and their coherent character can be found in, e.g. Beron-Vera et al. (2018).

454 *4.3.1 The role of tides*

455 The difference in the January NCPDs between the NTE and CR (experiments #1 and 2, respectively,
456 see Table 1 and Fig. 6a and 6b) demonstrates that the tidal forcing considerably affects the accumulation
457 patterns on the shelf. At the surface, the largest differences between the two experiments occur along
458 the East Anglia Plume/Frisian Front and along the front in the Irish Sea (Fig. 6a). Obviously, the tidal
459 signal affects frontal-like structures. Further differences between the two experiments appear in the
460 English Channel, around the north of Great Britain/Fair Isle Current, and at the continental slope of the
461 Celtic Sea. In most of the remaining parts of the domain, these differences are rather small.

462

463 Nevertheless, tides also affect the accumulation of particles in the deep ocean, which is dominated
464 by sub-basin-scale eddies, as well as other areas in the Bay of Biscay and in the Norwegian
465 Trench/Skagerrak, which are dominated by mesoscale motions. This could serve as another indication
466 of the interaction between tides and mesoscale dynamics.

467

468 The most pronounced large-scale feature in the differences observed at the sea surface is in the
469 vicinity of the shelf (Fig. 6a). At the bottom (Fig. 6b), the largest differences between the two
470 experiments occur also beyond the 200 m isobaths in the direction of the open ocean. The changing
471 sign of the difference reflects large oscillations at small scales of O(grid size), possibly indicating that
472 a further increase in the model resolution is needed to adequately resolve the accumulation and
473 dispersion of particles in the area of the continental slope. Bottom patterns in the North Sea are also
474 present and clearly demonstrate the importance of tides as a driver of particle accumulation there. The
475 principal patterns are similar to the surface with differences around Great Britain but the difference
476 signal is more variable. In the Southern Bight and southern North Sea the difference patterns are rather
477 distinct and follow the flanks of the Dogger Bank and the East Anglia Plume. This comparison between
478 the surface and bottom patterns indicates that, unlike the currents, which do not drastically change in
479 the vertical direction in the shallow ocean, the accumulation of particles at the bottom is different from
480 that at the sea surface. This suggests that the tides modifies the particle accumulation patterns by the

481 induced shear diffusion. This finding is supported by the influence of tides on surface deformation
482 (compare Fig. 6a and 2h), the pattern of which partly coincides with the NCPD difference.
483
484 *4.3.2 The role of wind*
485 A large part of the variability of shelf dynamics is caused by atmospheric variability (mostly on synoptic
486 time scales) (Jacob and Stanev, 2017); therefore, we will analyse the contributions of wind to the
487 accumulation and dispersion of particles in the FWE and NWE (experiments #3 and 4, respectively, see
488 Table 1). It is worth noting that the ranges of the responses to wind variability are comparable to the
489 responses to tides. The overall conclusion from the comparison among the differences in the surface
490 properties between the NTE and CR (Fig. 6a) from one perspective and between the FWE and CR (Fig.
491 6c) from another perspective is that the largest differences caused by tides and winds occur in almost
492 the same areas: the Frisian and Irish Sea Fronts, the continental slope, and the Norwegian Trench,
493 whereas the English Channel is less influenced in FWE. Filtering the wind (FWE) also makes the
494 accumulation strips "sharper", whereas the short-term wind forcing tends to "blur" the particle
495 distribution. However, turning the wind off (NWE) changes the accumulation patterns significantly
496 (compare Fig. 6e and 6c). The most affected areas are (1) the coastal areas of Great Britain and Ireland,
497 (2) the Skagerrak, which no longer accumulates particles, (3) the mouths of the Rhine and Elbe rivers
498 which extend further to the west, and (4) the coasts of the Armorican Shelf. Reducing the variability of
499 the wind or turning it off completely also has very pronounced impacts on the bottom particles (compare
500 Fig. 6d and 6f). The strongest impacts on bottom accumulation patterns are located in the northern part
501 of the shelf and the Norwegian Trench/Skagerrak.
502
503 The difference between the FWE and NWE (not illustrated here) demonstrates that, on the shelf,
504 the westerlies are essential for particle accumulation (compare Fig. 6e with 6g and Fig. 6f with 6h).
505
506 *4.3.3 The role of fronts*
507 The high-salinity and high-temperature gradients (fronts) in Fig. 2d and 2f are similar to the NCPD
508 patterns shown in Fig. 5a. These fronts support the ones reported by Belkin et al. (2009), particularly

509 the fronts in the southern North Sea. Additionally, in terms of the yearly averaged NCPD (Fig. 5c), the
510 NCPD maxima coincide with the known front positions; in contrast, not all detected fronts show particle
511 accumulation. There are also some differences from the analysis of Pietrzak et al. (2011), who analysed
512 the dynamics of the Frisian Front and East Anglia Plume using satellite data of the SST and SPM. The
513 differences between the present simulations and the results of Pietrzak et al. (2011) occur as a missing
514 East Anglia Plume and are mostly because the particles in the model have a neutral buoyancy and
515 because no particle sources are prescribed (the seeding is uniform).
516
517 To demonstrate the ability of a front to accumulate particles, a surface section across the Rhine
518 Plume (Frisian Front) is chosen as an example (solid black line in Fig. 5a; see also its inset). The front
519 separates the waters of the English Channel (higher salinity) and the Rhine ROFI (lower salinity). In
520 Fig. 7, the graphs start in the west (left) and end in the east (right). The maximum NCPD in the CR (left
521 vertical dashed line) is located where the salinity and temperature start to decrease (~34.6 to 28.7 PSU
522 and ~7.6 to 5.3°C, respectively). The related density changes are ~4.62 and 0.28 kg m^{-3}. Hence, the
523 salinity causes the density gradient which in turn influences the accumulation of particles. In the
524 backward simulation (CR-B; experiment #5, see Table 1), the NCPD maximum (right vertical dashed
525 line) is at the same location with respect to the salinity change when the particles are coming from the
526 opposite direction. Due to the residual currents, in the CR the particles come from the southwest and in
527 the CR-B from the northeast. The peaks of the NCPD curves are bounded by a rather constant NCPD,
528 which is higher on the side of particle supply than on the side of particle dispersion in the CR. In the
529 CR-B, the particle supply is reduced by the front, because only particles from the German Bight and
530 the Danish coastal region can reach the front. These regions are relatively small compared to the whole
531 North Sea being the particle supplier in the CR. This implies that particle simulations in regions with
532 frontal systems are not fully reversible and backward simulations have to be interpreted carefully. In
533 terms of the position of NCPD maxima, the results of Fig. 7 are very similar to what has been found by
534 Flament and Armi (2000) and Lohmann and Belkin (2014). Despite the vertical dynamics (see Sect.
535 4.4), particle accumulation along fronts can be explained considering that the residual velocity is not
536 parallel to the front but oriented further clockwise (in the CR the orientation of the front is almost in the

537 north–south direction, whereas U is veered clockwise). This would lead to a crossing of the front by
538 particles, but the particles are hindered by the (haline) front and flow along it. In the CR-B, the dynamics
539 are reversed, and thus, particles accumulate on the other side of the front. Particle accumulation along
540 other ROFIs can also be observed at, e.g. the western Danish coast along the Elbe River outflow. Postma
541 (1984) called the boundary of the Wadden Sea a "line of no return" whose location is comparable to a
542 strong salinity gradient (Fig. 2c and 2d). From the results of the present study, this interpretation of the
543 boundary of the Wadden Sea can be confirmed: if a particle of the German Bight crosses the front, it is
544 unlikely that it will be able to return.
545
546 In the NWE (Fig. 6e), the Frisian and Irish Sea Fronts are less pronounced than in the CR,
547 demonstrating the intensification of frontal accumulation by wind. Due to the missing westerly wind,
548 particles are no longer transported to the fronts, where they can accumulate in the areas of thermohaline
549 gradients. This is especially true for regions where the wind is constantly blowing in the same direction,
550 e.g. regions within the westerlies.
551
552 Another kind of shelf front is a tidal mixing front (Sect. 3.1 and Fig. S2), whose dynamics have
553 been described repeatedly (e.g. Hill et al., 1993). These fronts are known to accumulate natural and
554 artificial flotsam (Simpson and Pingree, 1978). In July, tidal mixing fronts are clearly visible as
555 temperature gradients (Fig. S2a), and some of them can be observed in terms of NCPD patterns (Fig.
556 S2c). In contrast to January, these fronts disappear in July if the tides are turned off and demonstrate
557 their importance for particle accumulation in summer (Fig. S2d). Analyses of the January NTE results
558 (not shown) show almost no vanishing NCPD maxima implying that these maxima are not caused by
559 tides. Due to the seasonal occurrence, tidal mixing fronts are less pronounced in the yearly averaged
560 NCPD then others fronts, e.g. the fronts of ROFIs. However, not all of them occur as NCPD maxima.
561 Although the well-known jet-like velocities along fronts can be seen in U in Fig. 7, the horizontal model
562 resolution is probably too coarse; that is, the model cannot resolve all important frontal dynamics.
563
564 *4.4. Vertical circulation in the North Sea*

565 Although shelf dynamics are dominated by strong horizontal motions, they cannot be considered fully
566 two-dimensional. Examples of the role of vertical processes are given by tidal mixing fronts (Garret
567 and Loder, 1981; van Aken et al, 1987), upwelling in the German Bight (Krause et al., 1986), tidal
568 straining (de Boer et al., 2009) and secondary circulation in estuaries. The differences between the
569 surface and bottom accumulation patterns described in Sect. 4.3.3 (Fig. 5a and 5b) are indicative of the
570 role of vertical processes. Such indications are clearly observed in the map of the differences between
571 the vertical positions of particles released at the bottom after one month of integration (Fig. 8a).
572 Pronounced depth changes appear along the eastern British coast, eastern Irish coast, around the Dogger
573 Bank and in several smaller coastal areas, e.g. at the western French coast. Some of these patterns are
574 topographically induced, like the one at the Dogger Bank, where particles from the northwest ascend
575 and particles released on the Dogger Bank descend. However, a NCPD at the surface smaller than 1
576 and a NCPD at the bottom greater than 1 (compare Fig. 5c with 5d) suggest an upward movement of
577 water not being induced by topography. Single particle trajectories along the British coast reveal that
578 the bottom flow is directed coastward and offshore at the surface (small inset in Fig. 8a).
579
580 In the backtracking experiment (CR-B, experiment #5, see Table 1; Fig. 8b), particles accumulate
581 in coastal upwelling areas, emphasising the dynamics described above. The opposite situation is present
582 on the northwestern Irish coast and in the western Irish Sea; here, a downward movement of water can
583 be observed. The NWE shows that the main driver of coastal water transport at meridionally oriented
584 coasts is the prevailing westerlies (Fig. 6e and 6f). Without wind, the eastern Irish and British coasts
585 have NCPD values clearly exceeding 0.3; with the original wind forcing, these areas have NCPD values
586 smaller than 0.3. In contrast, the NCPD of the western Irish coast and in the western Irish Sea is reduced
587 in the NWE. These results also support the theory of Lentz and Fewings (2012) regarding wind-driven
588 inner-shelf circulation.
589
590 Wind forcing is not the only explanation for the offshore-directed transport at some of the shelf
591 coasts, particularly along the eastern British coast, e.g. the Flamborough Head tidal mixing front.
592 Downwelling at fronts is associated with upwelling on the coastward side as a result of coastward

593 transport at the bottom and offshore-directed transport at the surface. Similar effects have been modelled
594 (Garret and Loder, 1981) and observed (van Aken et al., 1987) in previous studies.
595
596 *4.5 Dynamics at the shelf edge*
597 The analysis below uses the results of the CR-V (experiment #6, see Table 1) with the seeding
598 prescribed in a 100 km wide segment extending oceanward from the 150 m isobaths. The exchange of
599 particles between the deep ocean and the shelf is estimated by the number of particles crossing the 200
600 m isobaths and the changes in their depth with respect to the depth at which they were released. The
601 100 km wide segment is divided vertically into four parts: from the surface to 100 m (Fig. 9a), 100–200
602 m (Fig. 9b), 200–300 m (Fig. 9c) and 900–1,000 m (Fig. 9d). The major result of this experiment is that
603 with increasing depth (1) the dispersion of the cloud of particles in the vicinity of the 200 m isobaths
604 decreases, and (2) particles in the deeper layers do not penetrate onto the shelf. Many particles released
605 above 100 m move onto the shelf; their depth remains almost unchanged or even decreases (Fig. 9a).
606 In the three deeper intervals of release, deep oceanward transport is dominant (red stripe along the 200
607 m isobath in Fig. 9b, c and d). These dynamics, which are sketched in Fig. 9e, support the results of
608 Holt et al. (2009), Huthnance et al. (2009) and Graham et al (2018), whose simulations also showed
609 shelfward transport distinctive of the upper 150 m along the 200 m isobath; below 150 m, they found
610 deep oceanward transport. The simulated exchanges between the shelf and open ocean (the extent and
611 direction of particle propagation) are also in overall agreement with the recent results of Marsh et al.
612 (2017), who analysed drifter observations and Lagrangian simulations at the ENWS continental slope.
613 Down to 300 m, particles propagating away from the continental slope form filaments and eddy-like
614 patterns as in the Bay of Biscay; another fraction of the particles are advected within the slope current.
615 Although the latter are covered by the coloured areas, some of them are visible at the entrance of the
616 Norwegian Trench. The underlying dynamics at the ENWS continental slope are discussed in Sect. 4.1
617 and 4.2.
618
619 **5 Conclusions**

620 Numerical experiments were carried out with NEMO, in which a Lagrangian module was incorporated
621 in order to learn more about the ocean dynamics on the Northwest European Shelf. Lagrangian analyses
622 in conjunction with Eulerian analyses revealed physically distinct regimes in different parts of the study
623 area. The underlying dynamics were investigated in terms of accumulation and removal of neutrally
624 buoyant particles solely advected by the model velocities. To quantify accumulation and removal of
625 particles, a quantity named NCPD was introduced. The current knowledge about shelf and shelf edge
626 processes is extended not only by analysing specific processes but also by providing a rather
627 comprehensive description of the dynamics.
628
629 • On the shelf: Fronts act as barriers and accumulate particles. Tides affect the positions and
630 appearance of particle accumulation in frontal areas. Vertical water transport at meridionally
631 oriented coasts on the shelf is influenced by westerlies. Offshore-directed wind induces a NCPD
632 smaller than 1; the situation is reversed for onshore-directed wind.
633 • In the deep ocean: Eddies influence the particle dynamics on short time scales (individual
634 months); however, an annual mean of NCPD $\approx$ 1 reveals the absence of long-term stable
635 accumulation areas. In the Bay of Biscay accumulation patterns form on longer time scales than
636 one month. Tides affect the NCPD, suggesting the interaction of tides and mesoscale dynamics.
637 • Shelf edge (200 m isobath): The shelf edge represents a transition zone from the wind- and
638 tidally driven shallow shelf regime to a baroclinic eddy-dominated deep ocean regime. The
639 shelf edge shows on-shelf transport in the upper layers and downwelling-like off-shelf-directed
640 transport below 100 m. Bottom current branches tend to remove particles from the continental
641 slope.
642 • At the surface: Accumulation patterns on the shelf show high variability on monthly time
643 scales; some accumulation areas remain stable on yearly average of monthly patterns. These
644 long-term stable zones occur mainly along the fronts of ROFIs and in the Skagerrak. At the
645 shelf edge, particles are transported onto the shelf by westerlies. The influence of wind
646 variability on particle accumulation is of the order of the influence of tides.

- At the bottom: On the shelf, bottom currents are mainly influenced by the topography and follow its thalweg.

The differences in the properties of the velocity field (e.g. deformation) reveal two different regimes: a shelf regime with rather little deformation and a deep ocean regime at the 10-km scale with considerable deformation. On the shelf, tidally induced deformation plays an important role in particle accumulation and dispersal. The major hypothesis in the present study, that the vertical circulation in the shallow North Sea plays a substantial role, was confirmed.

The present study demonstrates the illustrative potential of Lagrangian methods. In conjunction with traditional Eulerian analysis, Lagrangian analysis can enhance the interpretation of observed or simulated dynamics and provide a solid basis for estimating the propagation of floating marine debris.

Code/data availability: The model codes of NEMO (https://www.nemo-ocean.eu), ARIANE (stockage.univ-brest.fr/~grima/Ariane/) and OpenDrift (https://github.com/OpenDrift/opendrift) as well as the GPS drifter (Carrasco and Horstmann, 2017), FOAM AMM7 (marine.copernicus.eu), HF radar (http://codm.hzg.de/codm/) and OSTIA (marine.copernicus.eu) data are freely available. E-HYPE data can be accessed under https://hypeweb.smhi.se/ and the NWP model data under https://www.metoffice.gov.uk/. Scripts and model output can be obtained by a request to the corresponding author.

Author contributions. MR and EVS conceived the study. MR performed the model runs and analyses and prepared the figures. MR and EVS interpreted the results, and MR prepared the manuscript with a significant contribution from EVS.

Competing interests. The authors declare that they have no conflicts of interest.

Acknowledgments. We thank the UK Met Office and Joanna Staneva for providing the NEMO AMM7 setup. This study was carried out within the project "Macroplastics Pollution in the Southern North Sea – Sources, Pathways and Abatement Strategies" (grant no. ZN3176) funded by the German Federal State of Lower Saxony. The authors thank Sebastian Grayek for technical support and Jens Meyerjürgens for carefully reading the manuscript and giving important advice. We appreciate the two anonymous reviewers for their critical and detailed comments.

References

van Aken, H. M. (2001). The hydrography of the mid-latitude Northeast Atlantic Ocean — Part III: the subducted thermocline water mass. *Deep Sea Res. Pt. I: Oceanographic Research Papers*, *48*(1), 237–267. https://doi.org/10.1016/S0967-0637(00)00059-5

van Aken, H. M., van Heijst, G. J. F., & Maas, L. R. M. (1987). Observations of fronts in the North Sea. *J. Mar. Res.*, *45*(3), 579–600. https://doi.org/10.1357/002224087788326830

Backhaus, J. (1979). First Results of a Three-Dimensional Model on the Dynamics in the German Bighta. In J. C. J. Nihoul (Ed.), *Elsev. Oceanogr. Serie.* (Vol. 25, pp. 333–349). Elsevier. https://doi.org/10.1016/S0422-9894(08)71138-3

Backhaus, J. O. (1985). A three-dimensional model for the simulation of shelf sea dynamics. *Deutsche Hydrografische Zeitschrift*, *38*(4), 165–187. https://doi.org/10.1007/BF02328975

Baschek, B., Schroeder, F., Brix, H., Riethmuller, R., Badewien, T.H., Breitbach, G., et al. (2017). The coastal observing system for northern and arctic seas (COSYNA). Ocean Sci. *13*(3), 379–410. https://doi.org/10.5194/os-13-379-2107

Belkin, I. M., Cornillon, P. C., & Sherman, K. (2009). Fronts in Large Marine Ecosystems. *Prog. Oceanogr.*, *81*(1), 223–236. https://doi.org/10.1016/j.pocean.2009.04.015

Beron-Vera, F. J., Hadjighasem, A., Xia, Q., Olascoaga, M. J., & Haller, G. (2018). Coherent Lagrangian swirls among submesoscale motions. *P. Natl. Acad. Sci. USA*, 201701392. https://doi.org/10.1073/pnas.1701392115

Blanke, B., & Raynaud, S. (1997). Kinematics of the Pacific Equatorial Undercurrent: An Eulerian and Lagrangian Approach from GCM Results. *J. Phys. Oceanogr.*, *27*(6), 1038–1053. https://doi.org/10.1175/1520-0485(1997)027<1038:KOTPEU>2.0.CO;2

Blanke, B., Arhan, M., Madec, G., & Roche, S. (1999). Warm Water Paths in the Equatorial Atlantic as Diagnosed with a General Circulation Model. *J. Phys. Oceanogr.*, *29*(11), 2753–2768. https://doi.org/10.1175/1520-0485(1999)029<2753:WWPITE>2.0.CO;2

de Boer, G. J., Pietrzak, J. D., & Winterwerp, J. C. (2009). SST observations of upwelling induced by tidal straining in the Rhine ROFI. *Cont. Shelf Res.*, *29*(1), 263–277. https://doi.org/10.1016/j.csr.2007.06.011

Booth, D. A. (1988). Eddies in the Rockall Trough. *Oceanologica Acta*, *11*(3), 213–219.

Bower, A. S., Lozier, M. S., Gary, S. F., & Böning, C. W. (2009). Interior pathways of the North Atlantic meridional overturning circulation. *Nature*, *459*(7244), 243–247. https://doi.org/10.1038/nature07979

Brown, J., Hill, A. E., Fernand, L., & Horsburgh, K. J. (1999). Observations of a Seasonal Jet-like Circulation at the Central North Sea Cold Pool Margin. *Estuar. Coast. Shelf S.*, *48*(3), 343–355. https://doi.org/10.1006/ecss.1999.0426

Brown, J., Carrillo, L., Fernand, L., Horsburgh, K. J., Hill, A. E., Young, E. F., & Medler, K. J. (2003). Observations of the physical structure and seasonal jet-like circulation of the Celtic Sea and St. George's Channel of the Irish Sea. *Cont.l Shelf Res.*, *23*(6), 533–561. https://doi.org/10.1016/S0278-4343(03)00008-6

Callies, U., Plüß, A., Kappenberg, J., & Kapitza, H. (2011). Particle tracking in the vicinity of Helgoland, North Sea: a model comparison. *Ocean Dynam.*, *61*(12), 2121–2139. https://doi.org/10.1007/s10236-011-0474-8

Callies, U., Groll, N., Horstmann, J., Kapitza, H., Klein, H., Maßmann, S., & Schwichtenberg, F. (2017). Surface drifters in the German Bight: model validation considering windage and Stokes drift. *Ocean Science*, *13*(5), 799–827. https://doi.org/10.5194/os-13-799-2017

Carrasco, R., & Horstmann, J. (2017). *German Bight surface drifter data from Heincke cruise HE 445, 2015*, PANGAEA. https://doi.org/10.1594/PANGAEA.874511

729 Daewel, U., Peck, M. A., Kühn, W., St. John, M. A., Alekseeva, I., & Schrum, C. (2008). Coupling
730 ecosystem and individual-based models to simulate the influence of environmental variability on
731 potential growth and survival of larval sprat (Sprattus sprattus L.) in the North Sea. *Fish.*
732 *Oceanogr.*, *17*(5), 333–351. https://doi.org/10.1111/j.1365-2419.2008.00482.x
733 Dagestad, K.-F., Röhrs, J., Breivik, Ø., & Ådlandsvik, B. (2018). OpenDrift v1.0: a generic
734 framework for trajectory modelling. *Geosci. Model Dev.*, *11*(4), 1405–1420.
735 https://doi.org/10.5194/gmd-11-1405-2018
736 Davies, A. M, & Xing, J. (2001). Modelling processes influencing shelf edge currents, mixing, across
737 shelf exchange, and sediment movement at the shelf edge. *Dynam. Atmos. Oceans*, *34*(2), 291–
738 326. https://doi.org/10.1016/S0377-0265(01)00072-0
739 Davies, A. M., Sauvel, J., & Evans, J. (1985). Computing near coastal tidal dynamics from
740 observations and a numerical model. *Cont. Shelf Res.*, *4*(3), 341–366.
741 https://doi.org/10.1016/0278-4343(85)90047-0
742 Donlon, C. J., Martin, M., Stark, J., Roberts-Jones, J., Fiedler, E., & Wimmer, W. (2012). The
743 Operational Sea Surface Temperature and Sea Ice Analysis (OSTIA) system. *Remote Sensing of*
744 *Environment*, *116*, 140–158. https://doi.org/10.1016/j.rse.2010.10.017
745 Flament, P., & Armi, L. (2000). The Shear, Convergence, and Thermohaline Structure of a Front.
746 *Journal of Physical Oceanography*, *30*(1), 51–66. https://doi.org/10.1175/1520-
747 0485(2000)030<0051:TSCATS>2.0.CO;2
748 Flather, R. A. (1994). A Storm Surge Prediction Model for the Northern Bay of Bengal with
749 Application to the Cyclone Disaster in April 1991. *Journal of Physical Oceanography*, *24*(1),
750 172–190. https://doi.org/10.1175/1520-0485(1994)024<0172:ASSPMF>2.0.CO;2
751 Froyland, G., Stuart, R. M., & van Sebille, E. (2014). How well-connected is the surface of the global
752 ocean? *Chaos*, *24*(3), 033126. https://doi.org/10.1063/1.4892530
753 Garrett, C. J. R., & Loder, J. W. (1981). Circulation and fronts in continental shelf seas - Dynamical
754 aspects of shallow sea fronts. *Philos. T. Roy. Soc. A*, *302*(1472), 563–581.
755 https://doi.org/10.1098/rsta.1981.0183

Graham, J. A., Rosser, J. P., O'Dea, E., & Hewitt, H. T. (2018). Resolving Shelf Break Exchange Around the European Northwest Shelf. *Geophysical Research Letters*, *45*(22), 12,386-12,395. https://doi.org/10.1029/2018GL079399

Guihou, K., Polton, J., Harle, J., Wakelin, S., O'Dea, E., & Holt, J. (2018). Kilometric Scale Modeling of the North West European Shelf Seas: Exploring the Spatial and Temporal Variability of Internal Tides. *J. Geophys. Res.-Oceans*, *122*. https://doi.org/10.1002/2017JC012960

Gutow, L., Ricker, M., Holstein, J., Dannheim, J., Stanev, E. V. & Wolff, J.-O. (2018). Distribution and trajectories of floating and benthic marine macrolitter in the south-eastern North Sea. *Mar. Pollut. Bull.*, *131*, *Part A*, 763–772. https://doi.org/10.1016/j.marpolbul.2018.05.003

Hainbucher, D., Pohlmann, T., & Backhaus, J. (1987). Transport of conservative passive tracers in the North Sea: first results of a circulation and transport model. *Cont. Shelf Res.*, *7*(10), 1161–1179. https://doi.org/10.1016/0278-4343(87)90083-5

Haller, G., & Yuan, G. (2000). Lagrangian coherent structures and mixing in two-dimensional turbulence. *Physica D*, *147*(3), 352–370. https://doi.org/10.1016/S0167-2789(00)00142-1

Heaps, N. S. (1980). Density currents in a two-layered coastal system, with application to the Norwegian Coastal Current. *Geophys. J. Roy. Astr. S.*, *63*(2), 289–310. https://doi.org/10.1111/j.1365-246X.1980.tb02622.x

Hill, A. E., James, I. D., Linden, P. F., Matthews, J. P., Prandle, D., Simpson, J. H., et al. (1993). Understanding the North Sea system - Dynamics of tidal mixing fronts in the North Sea. *Philos. T. Roy. Soc. A*, *343*(1669), 431–446. https://doi.org/10.1098/rsta.1993.0057

Hill, A. E., Brown, J., Fernand, L., Holt, J., Horsburgh, K. J., Proctor, R., Raine, R., & Turrell, W. R. (2008). Thermohaline circulation of shallow tidal seas. *Geophys. Res. Lett.*, *35*(11), L11605. https://doi.org/10.1029/2008GL033459

Holmström, A. (1975). Plastic films on the bottom of the Skagerack. *Nature*, *255*(5510), 622–623. https://doi.org/10.1038/255622a0

Holt, J. T., & James, I. D. (1999). A simulation of the Southern North Sea in comparison with measurements from the North Sea Project. Part 1: Temperature. *Cont. Shelf Res.*, *19*(8), 1087–1112. https://doi.org/10.1016/S0278-4343(99)00015-1

784 Holt, J., & Umlauf, L. (2008). Modelling the tidal mixing fronts and seasonal stratification of the
785 Northwest European Continental shelf. *Cont. Shelf Res.*, *28*(7), 887–903.
786 https://doi.org/10.1016/j.csr.2008.01.012
787 Holt, J., Wakelin, S., & Huthnance, J. (2009). Down-welling circulation of the northwest European
788 continental shelf: A driving mechanism for the continental shelf carbon pump. *Geophysical*
789 *Research Letters*, *36*(14), L14602. https://doi.org/10.1029/2009GL038997
790 Howarth, M. J. (2001). North Sea Circulation. In J. H. Steele, K. K. Turekian, & S. A. Thorpe (Eds.),
791 *Encyclopedia of Ocean Sciences: Vol. 1* (1st edition, pp. 1912–1921). Oxford: Academic Press.
792 Huntley, H. S., Lipphardt, B. L., Jacobs, G., & Kirwan, A. D. (2015). Clusters, deformation, and
793 dilation: Diagnostics for material accumulation regions. *Journal of Geophysical Research:*
794 *Oceans*, *120*(10), 6622–6636. https://doi.org/10.1002/2015JC011036
795 Huthnance, J. M. (1991). Physical oceanography of the North Sea. *Ocean and Shoreline Management*,
796 *16*(3), 199–231. https://doi.org/10.1016/0951-8312(91)90005-M
797 Huthnance, J. M. (1995). Circulation, exchange and water masses at the ocean margin: the role of
798 physical processes at the shelf edge. *Prog. Oceanogr., 35*(4), 353–431.
799 https://doi.org/10.1016/0079-6611(95)80003-C
800 Huthnance, J. M., Holt, J. T., & Wakelin, S. L. (2009). Deep ocean exchange with west-European
801 shelf seas. *Ocean Sci.*, *5*(4), 621–634. https://doi.org/10.5194/os-5-621-2009
802 Jacob, B., & Stanev, E. V. (2017). Interactions between wind and tidally induced currents in coastal
803 and shelf basins. *Ocean Dynam.*, *67*(10), 1263–1281. https://doi.org/10.1007/s10236-017-1093-9
804 Jacobs, G. A., Huntley, H. S., Kirwan, A. D., Lipphardt, B. L., Campbell, T., Smith, T., Edwards, K.,
805 & Bartels, B. (2016). Ocean processes underlying surface clustering. *J. Geophys. Res. Oceans*,
806 *121*(1), 180–197. https://doi.org/10.1002/2015JC011140
807 Krause, G., Budeus, G., Gerdes, D., Schaumann, K., & Hesse, K. (1986). Frontal Systems in the
808 German Bight and their Physical and Biological Effects. In J. C. J. Nihoul (Ed.), *Elsev. Oceanogr.*
809 *Serie.* (Vol. 42, pp. 119–140). Elsevier. https://doi.org/10.1016/S0422-9894(08)71042-0
810 Koszalka, I. M., & LaCasce, J. H. (2010). Lagrangian analysis by clustering. *Ocean Dynam.*, *60*(4),
811 957–972. https://doi.org/10.1007/s10236-010-0306-2

812 Koszalka, I. M., LaCasce, J. H., Andersson, M., Orvik, K. A., & Mauritzen, C. (2011). Surface
813 circulation in the Nordic Seas from clustered drifters. *Deep Sea Research Part I: Oceanographic*
814 *Research Papers*, *58*(4), 468–485. https://doi.org/10.1016/j.dsr.2011.01.007
815 Le Fèvre, J. (1986). Aspects of the Biology of Frontal Systems. *Adv. Mar. Biol.*, *23*, 163–299.
816 Lentz, S. J., & Fewings, M. R. (2012). The wind- and wave-driven inner-shelf circulation. *Annu. Rev.*
817 *Mar. Sci.*, *4*(1), 317–343. https://doi.org/10.1146/annurev-marine-120709-142745
818 Lohmann, R., & Belkin, I. M. (2014). Organic pollutants and ocean fronts across the Atlantic Ocean:
819 A review. *Prog. Oceanogr.*, *128*(Supplement C), 172–184.
820 https://doi.org/10.1016/j.pocean.2014.08.013
821 Madec, G. (2008). NEMO ocean engine. *Note du Pôle de modélisation, Institut Pierre-Simon Laplace*
822 *(IPSL), France*, (27).
823 Mahadevan, A. (2016). The Impact of Submesoscale Physics on Primary Productivity of Plankton.
824 *Annu. Rev. Mar. Sci.*, *8*, 161–184. https://doi.org/10.1146/annurev-marine-010814-015912
825 Maier-Reimer, E. (1977). Residual circulation in the North Sea due to the M2-tide and mean annual
826 wind stress. *Deutsche Hydrografische Zeitschrift*, *30*(3), 69–80.
827 https://doi.org/10.1007/BF02227045
828 Marsh, R., Haigh, I. D., Cunningham, S. A., Inall, M. E., Porter, M., & Moat, B. I. (2017). Large-
829 scale forcing of the European Slope Current and associated inflows to the North Sea. *Ocean Sci.*,
830 *13*(2), 315–335. https://doi.org/10.5194/os-13-315-2017
831 Maximenko, N., Hafner, J., Kamachi, M., & MacFadyen, A. (2018). Numerical simulations of debris
832 drift from the Great Japan Tsunami of 2011 and their verification with observational reports. *Mar.*
833 *Pollut. Bull.*, *132*, 5–25. https://doi.org/10.1016/j.marpolbul.2018.03.056
834 McWilliams, J. C. (2016). Submesoscale currents in the ocean. *P. Roy. Soc. A-Math. Phy.*, *472*(2189),
835 20160117. https://doi.org/10.1098/rspa.2016.0117
836 van der Molen, J., García-García, L. M., Whomersley, P., Callaway, A., et al. (2018). Connectivity of
837 larval stages of sedentary marine communities between hard substrates and offshore structures in
838 the North Sea. *Scientific Reports*, *8*(1), 14772. https://doi.org/10.1038/s41598-018-32912-2

839 Molinari, R., & Kirwan, A. D. (1975). Calculations of Differential Kinematic Properties from
840 Lagrangian Observations in the Western Caribbean Sea. *J. Phys. Oceanogr.*, *5*(3), 483–491.
841 https://doi.org/10.1175/1520-0485(1975)005<0483:CODKPF>2.0.CO;2
842 Neumann, D., Callies, U., & Matthies, M. (2014). Marine litter ensemble transport simulations in the
843 southern North Sea. *Mar. Pollut. Bull.*, *86*(1), 219–228.
844 https://doi.org/10.1016/j.marpolbul.2014.07.016
845 O'Dea, E. J., Arnold, A. K., Edwards, K. P., Furner, R., Hyder, P., Martin, M. J., Siddorn, J. R., et al.
846 (2012). An operational ocean forecast system incorporating NEMO and SST data assimilation for
847 the tidally driven European North-West shelf. *J. Oper. Oceanogr.*, *5*(1), 3–17.
848 https://doi.org/10.1080/1755876X.2012.11020128
849 O'Dea, E. J., Furner, R., Wakelin, S., Siddorn, J., While, J., Sykes, P., et al. (2017). The CO5
850 configuration of the 7 km Atlantic Margin Model: large-scale biases and sensitivity to forcing,
851 physics options and vertical resolution. *Geosci. Model Dev.*, *10*(8), 2947–2969.
852 https://doi.org/10.5194/gmd-10-2947-2017
853 Onink, V., Wichmann, D., Delandmeter, P., & Van Sebille, E. (n.d.). The Role of Ekman Currents,
854 Geostrophy, and Stokes Drift in the Accumulation of Floating Microplastic. *J. Geophys. Res.-*
855 *Oceans*, *124*(3), 1474–1490. https://doi.org/10.1029/2018JC014547
856 Otto, L., Zimmerman, J. T. F., Furnes, G. K., Mork, M., Saetre, R., & Becker, G. (1990). Review of
857 the physical oceanography of the North Sea. *Neth. J. Sea Res.*, *26*(2), 161–238.
858 https://doi.org/10.1016/0077-7579(90)90091-T
859 Paparella, F., Babiano, A., Basdevant, C., Provenzale, A., & Tanga, P. (1997). A Lagrangian study of
860 the Antarctic polar vortex. *J. Geophys. Res.-Atmos.*, *102*(D6), 6765–6773.
861 https://doi.org/10.1029/96JD03377
862 Pätsch, J., Burchard, H., Dieterich, C., Gräwe, U., Gröger, M., Mathis, M., et al. (2017). An
863 evaluation of the North Sea circulation in global and regional models relevant for ecosystem
864 simulations. *Ocean Model.*, *116*(Supplement C), 70–95.
865 https://doi.org/10.1016/j.ocemod.2017.06.005

866 Pietrzak, J. D., de Boer, G. J., & Eleveld, M. A. (2011). Mechanisms controlling the intra-annual
867 mesoscale variability of SST and SPM in the southern North Sea. *Cont. Shelf Res.*, *31*(6), 594–
868 610. https://doi.org/10.1016/j.csr.2010.12.014
869 Pingree, R. D., & Griffiths, D. K. (1978). Tidal fronts on the shelf seas around the British Isles. *J.*
870 *Geophys. Res.-Oceans*, *83*(C9), 4615–4622. https://doi.org/10.1029/JC083iC09p04615
871 Pohlmann, T. (2006). A meso-scale model of the central and southern North Sea: Consequences of an
872 improved resolution. *Cont. Shelf Res.*, *26*(19), 2367–2385.
873 https://doi.org/10.1016/j.csr.2006.06.011
874 Porter, M., Inall, M. E., Green, J. A. M., Simpson, J. H., Dale, A. C., & Miller, P. I. (2016). Drifter
875 observations in the summer time Bay of Biscay slope current. *Journal of Marine Systems*, *157*,
876 65–74. https://doi.org/10.1016/j.jmarsys.2016.01.002
877 Postma, H. (1984). Introduction to the symposium on organic matter in the Wadden Sea. In R. W. P.
878 M. Laane & W. J. Wolff (Eds.), *The role of organic matter in the Wadden Sea* (pp. 15–22). Texel,
879 Netherlands.
880 Reisser, J., Shaw, J., Wilcox, C., Hardesty, B. D., Proietti, M., Thums, M., & Pattiaratchi, C. (2013).
881 Marine Plastic Pollution in Waters around Australia: Characteristics, Concentrations, and
882 Pathways. *PLOS ONE*, *8*(11), e80466. https://doi.org/10.1371/journal.pone.0080466
883 Rodhe, J. (1987). The large-scale circulation in the Skagerrak; interpretation of some observations.
884 *Tellus A*, *39A*(3), 245–253. https://doi.org/10.1111/j.1600-0870.1987.tb00305.x
885 Röhrs, J., Christensen, K. H., Hole, L. R., Broström, G., Drivdal, M., & Sundby, S. (2012).
886 Observation-based evaluation of surface wave effects on currents and trajectory forecasts. *Ocean*
887 *Dynam.*, *62*(10–12), 1519–1533. https://doi.org/10.1007/s10236-012-0576-y
888 Rolinski, S. (1999). On the dynamics of suspended matter transport in the tidal river Elbe: Description
889 and results of a Lagrangian model. *J. Geophys. Res.-Oceans*, *104*(C11), 26043–26057.
890 https://doi.org/10.1029/1999JC900230
891 Schönfeld, W. (1995). Numerical simulation of the dispersion of artificial radionuclides in the English
892 Channel and the North Sea. *J. Marine Syst.*, *6*(5), 529–544. https://doi.org/10.1016/0924-
893 7963(95)00022-H

van Sebille, E., England, M. H., & Froyland, G. (2012). Origin, dynamics and evolution of ocean garbage patches from observed surface drifters. *Environmental Research Letters*, *7*(4), 044040. https://doi.org/10.1088/1748-9326/7/4/044040

van Sebille, E., Wilcox, C., Lebreton, L., Maximenko, N., Hardesty, B. D., van Franeker, J. A., et al. (2015). A global inventory of small floating plastic debris. *Environmental Research Letters*, *10*(12), 124006. https://doi.org/10.1088/1748-9326/10/12/124006

van Sebille, E., Griffies, S. M., Abernathey, R., Adams, T. P., Berloff, P., Biastoch, A., Blanke, B., et al. (2018). Lagrangian ocean analysis: Fundamentals and practices. *Ocean Model.*, *121*, 49–75. https://doi.org/10.1016/j.ocemod.2017.11.008

Simpson, J. H., & Hunter, J. R. (1974). Fronts in the Irish Sea. *Nature*, *250*(5465), 404–406. https://doi.org/10.1038/250404a0

Simpson, J. H., & Pingree, R. D. (1978). Shallow Sea Fronts Produced by Tidal Stirring. In *Oceanic Fronts in Coastal Processes* (pp. 29–42). Berlin: Springer. https://doi.org/10.1007/978-3-642-66987-3_5

Simpson, J. H., & Sharples, J. (2012). *Introduction to the Physical and Biological Oceanography of Shelf Seas*. Cambridge: Cambridge University Press.

Smagorinsky, J. (1963). General circulation experiments with the primitive equations. *Mon. Weather Rev.*, *91*(3), 99–164. https://doi.org/10.1175/1520-0493(1963)091<0099:GCEWTP>2.3.CO;2

Stanev, E. V., & Ricker, M. (2020). Interactions between barotropic tides and mesoscale processes in deep ocean and shelf regions. Accepted in *Ocean Dynam.*

Stanev, E. V., Schulz-Stellenfleth, J., Staneva, J., Grayek, S., Grashorn, S., Behrens, A., Koch, W. & Pein, J. (2016). Ocean forecasting for the German Bight: from regional to coastal scales. *Ocean Sci.*, *12*(5), 1105–1136. https://doi.org/10.5194/os-12-1105-2016

Stanev, E. V., Badewien, T. H., Freund, H., Grayek, S., Hahner, F., Meyerjürgens, J., Ricker, M., et al. (2019). Extreme westward surface drift in the North Sea: Public reports of stranded drifters and Lagrangian tracking. *Cont. Shelf Res.*, *177*, 24–32. https://doi.org/10.1016/j.csr.2019.03.003

Stanev, E. V., Ziemer, F., Schulz-Stellenfleth, J., Seemann, J., Staneva, J., & Gurgel, K. W. (2015). Blending Surface Currents from HF Radar Observations and Numerical Modelling: Tidal

922 Hindcasts and Forecasts, *J. Atmos. Ocean. Tech.*, *32*(2), 256–281. https://doi.org/10.1175/JTECH-
923 D-13-00164.1
924 Wakata, Y., & Sugimori, Y. (1990). Lagrangian Motions and Global Density Distributions of Floating
925 Matter in the Ocean Simulated Using Shipdrift Data. *J. Phys. Oceanogr.*, *20*(1), 125–138.
926 https://doi.org/10.1175/1520-0485(1990)020<0125:LMAGDD>2.0.CO;2
927 Zhang, Y. J., Stanev, E. V., & Grashorn, S. (2016). Unstructured-grid model for the North Sea and
928 Baltic Sea: Validation against observations. *Ocean Model.*, *97*, 91–108.
929 https://doi.org/10.1016/j.ocemod.2015.11.009

930 **Figure captions:**

931 **Fig. 1**. Bathymetry of the model domain. The shelf is defined as depths shallower than 200 m (colour
932 bar within the map). In this and all following figures, the 200 m depth contour is highlighted with a
933 black solid line. Grey arrows schematically show the general shelf sea circulation. The abbreviations
934 used in the text are as follows:
935 Armorican Shelf (*AS*), Bay of Biscay (*BB*), Celtic Sea (*CS*), Dogger Bank (*DB*), East Anglia (*EA*),
936 English Channel (*EC*), German Bight (*GB*), Goban Spur (*GS*), Irish Sea (*IS*), Kattegat (*Ka*), North Sea
937 (*NS*), Norwegian Trench (*NT*), Oyster Ground (*OG*), Rockall Trough (*RT*), Skagerrak (*Sk*), Southern
938 Bight (*SB*), St. George's Channel (*SGC*), Silver Pit (*SP*), Orkney/Shetland Islands (*OI*/*SI*), Outer
939 Hebrides (*OH*), Porcupine Bank (*PB*), Fair Isle Current (*a*), European Slope Current (*b*), East Anglia
940 Plume (*c*), Frisian Front (*d*), Rhine River (*1*), Ems River (*2*), Weser River (*3*) and Elbe River (*4*).
941
942 **Fig. 2.** Simulated surface properties in the control run (CR, #1, see Table 1) for January 2015: (a)
943 velocity magnitude derived from the averaged u and v velocity components, (b) mean velocity
944 magnitude, (c) mean salinity and (e) mean temperature. Magnitudes of the (d) temperature and (f)
945 salinity gradients as well as (g) the deformation in the CR and (h) the differences of the nontidal
946 experiment (NTE, #2) minus CR of the deformation are presented as 24.84-h averaged fields on 15
947 January 2015.
948
949 **Fig. 3**. Lagrangian trajectories of every 8th particle after 15 days of integration in the control run (CR,
950 #1, see Table 1) released on 1 January 2015. Particles are released at (a) the surface and (b) bottom.
951 (c) and (d) are magnified views of the domain showing all trajectories of (c) the first 12.42 h and (d)
952 24.00 h representative of different dynamics: (c) the area of the Armorican Shelf continental slope
953 including tidal ellipses and (d) the circulation in the Skagerrak. The trajectory colours are randomly
954 chosen for better visibility. Grey lines are isobaths in (c) 700-m and (d) 400-m steps.
955
956 **Fig. 4**. Particle positions after (a, b) 1 month and (c, d) 6 months released on 1 January 2015 at (a, c)
957 the surface and (b, d) bottom in the control run (CR, #1, see Table 1).

Fig. 5. Tendencies of accumulation shown as (a, b) the January mean normalised cumulative particle density (NCPD) and (c, d) the average of monthly NCPD for 2015 (averages of Fig. S5 and S6, respectively) in the control run (CR, #1, see Table 1). (a) and (c) correspond to surface-released particles, while (b) and (d) correspond to bottom-released particles . In (a), the solid black line located in the Southern Bight is the transect shown in Fig. 7 (enlarged in the inset). The numbers in (c) indicate the most pronounced accumulation areas.

Fig. 6. Analysis of the sensitivity experiments with respect to tides and wind. (a) and (b) are the differences of normalised cumulative particle density (NCPD) in the nontidal experiment (NTE, #2, see Table 1) minus the control run (CR, #1) in January 2015 at (a) the surface and (b) bottom. (c) and (d) are the corresponding differences between the filtered wind experiment (FWE, #3) and the CR; (e) and (f) are the differences between the nonwind wind experiment (NWE, #4) and the CR.

Fig. 7. Normalised cumulative particle density (NCPD), salinity (S), temperature (T) and residual velocity vectors (U) at the surface as the means of January 2015 along the transect in the Southern Bight (solid black line in Fig. 5a) in the control run (CR). The graph starts in the west and ends at the coast. The vertical dotted lines mark the NCPD maxima of the forward (left one, solid NCPD line) and backward (right one, dashed NCPD line) simulations (CR and CR-B, #1 and 5, respectively, see Table 1).

Fig. 8. (a) Difference of the final depth minus the initial depth of bottom-released particles after 1 month (January) in 2015 in the control run (CR, #1, see Table 1). Positive/negative values indicate a depth increase/decrease. The model grid in which a particle was released is coloured depending on its depth change. The small figure shows a magnified view of the British coast with two exemplary bottom (black) and surface (red) trajectories starting at the big dots. The trajectories are detided with a 25-h flowing mean. (b) Tendencies of accumulation shown as the January mean normalised cumulative particle density NCPD calculated from the backward simulation (CR-B, #5).

Fig. 9. Particle positions (purple dots) and particle depth differences with respect to the depth of release in different depth layers (colours) after 1 month (January) in 2015 computed in the control run with vertical particle seeding along the continental slope (CR-V, #6, see Table 1). Details of the seeding strategy can be found in Sect. 2.3. The colour coding shows the difference of the final depth minus the initial particle depth, computed as the mean difference of all particle depths seeded at the same location in the horizontal plane. All particles released in the respective depth range are taken into account. Particles were released in four depth layers: (a) 1–100 m, (b) 100–200 m, (c) 200–300 m and (d) 900–1,000 m. (e) Sketched dynamics at the continental slope concluded from (a) to (d).

Figures:

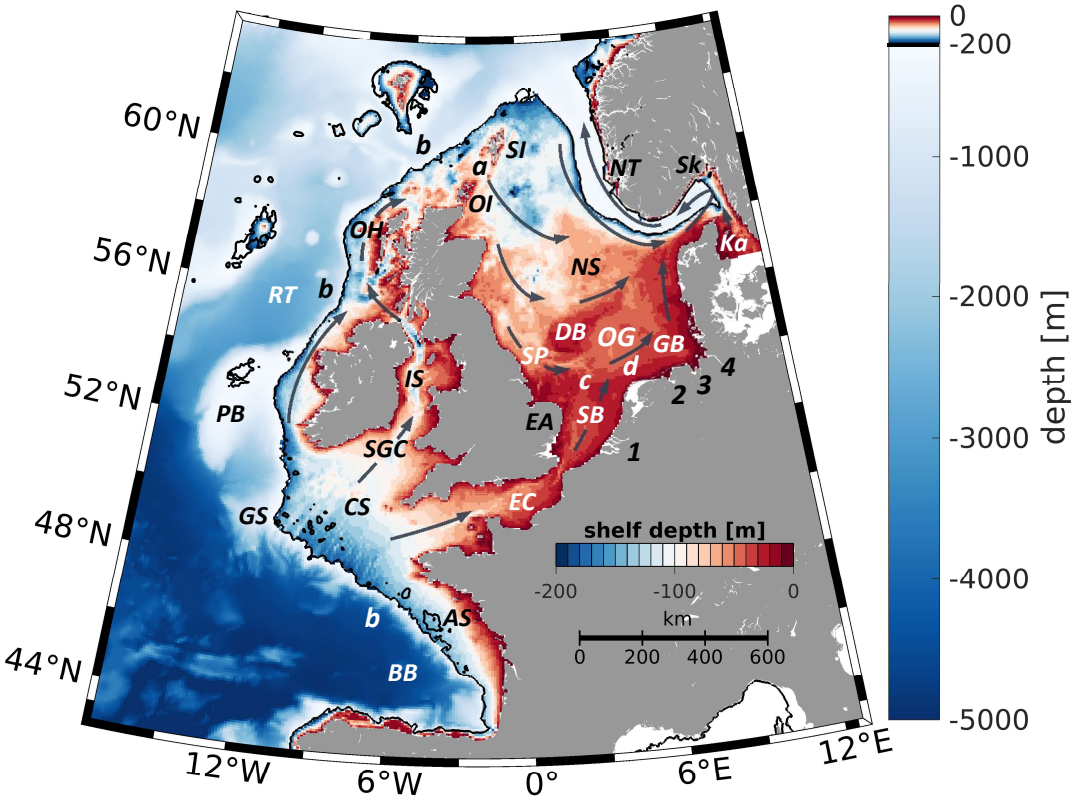

Fig. 1.

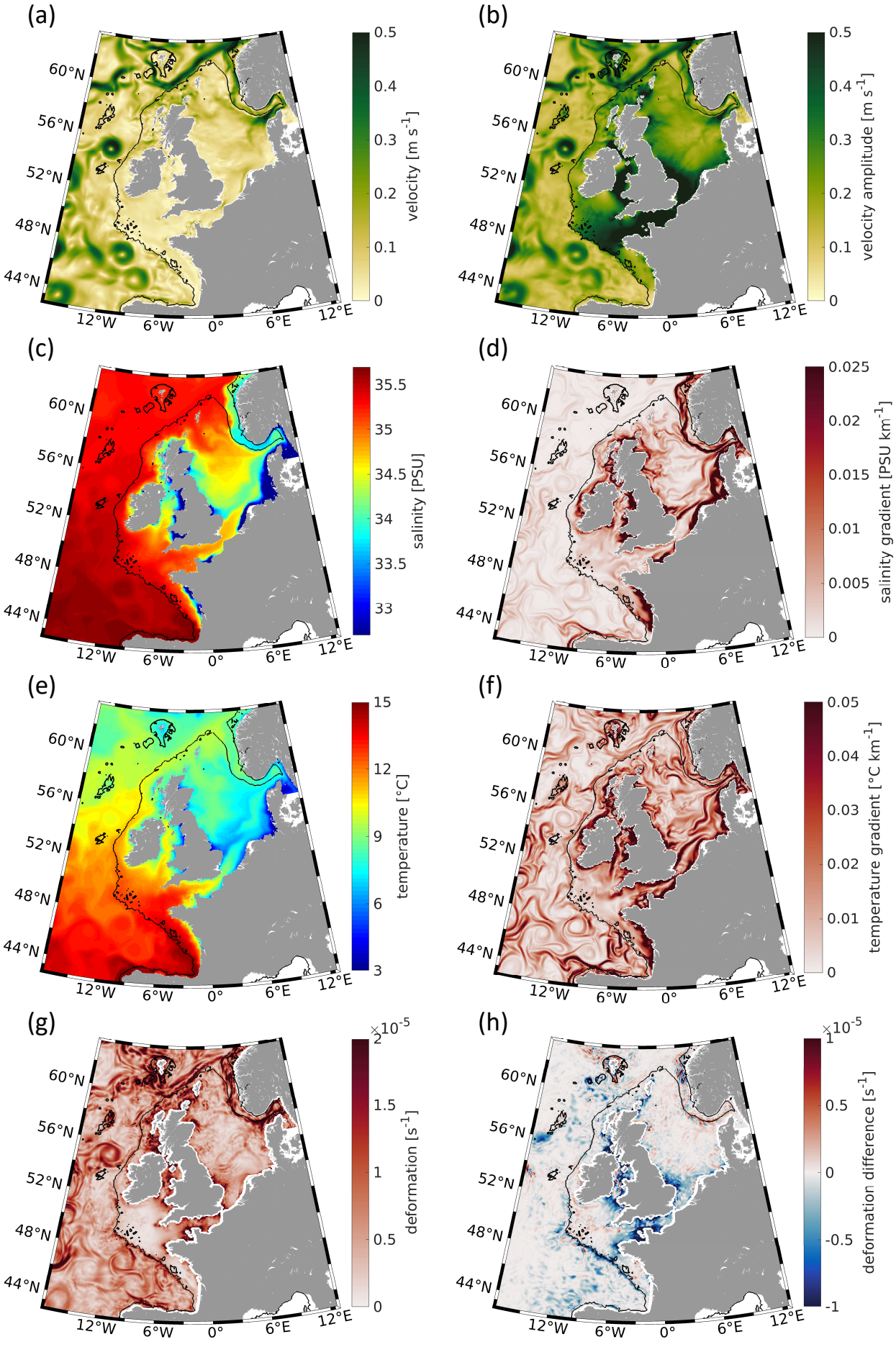
(a)
(b)
(c)
(d)
(e)
(f)
(g)
(h)
60°N
56°N
52°N
48°N
44°N
12°W
6°W
0°
6°E
12°E
velocity [m s-1]
velocity amplitude [m s-1]
salinity [PSU]
salinity gradient [PSU km-1]
temperature [°C]
temperature gradient [°C km-1]
deformation [s-1]
deformation difference [s-1]
×10-5

Fig. 2.

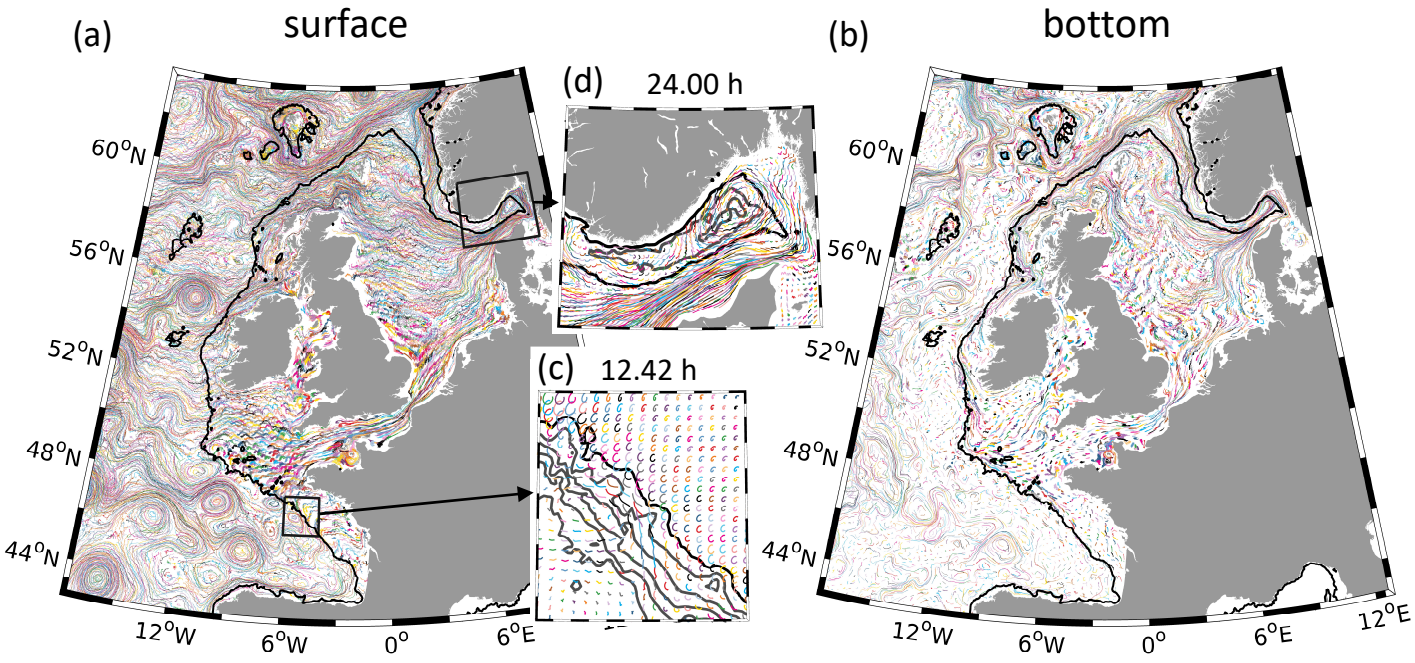
(a)
surface
(b)
bottom
(c) 12.42 h
(d) 24.00 h
60°N
56°N
52°N
48°N
44°N
12°W
6°W
0°
6°E
12°E

Fig. 3.

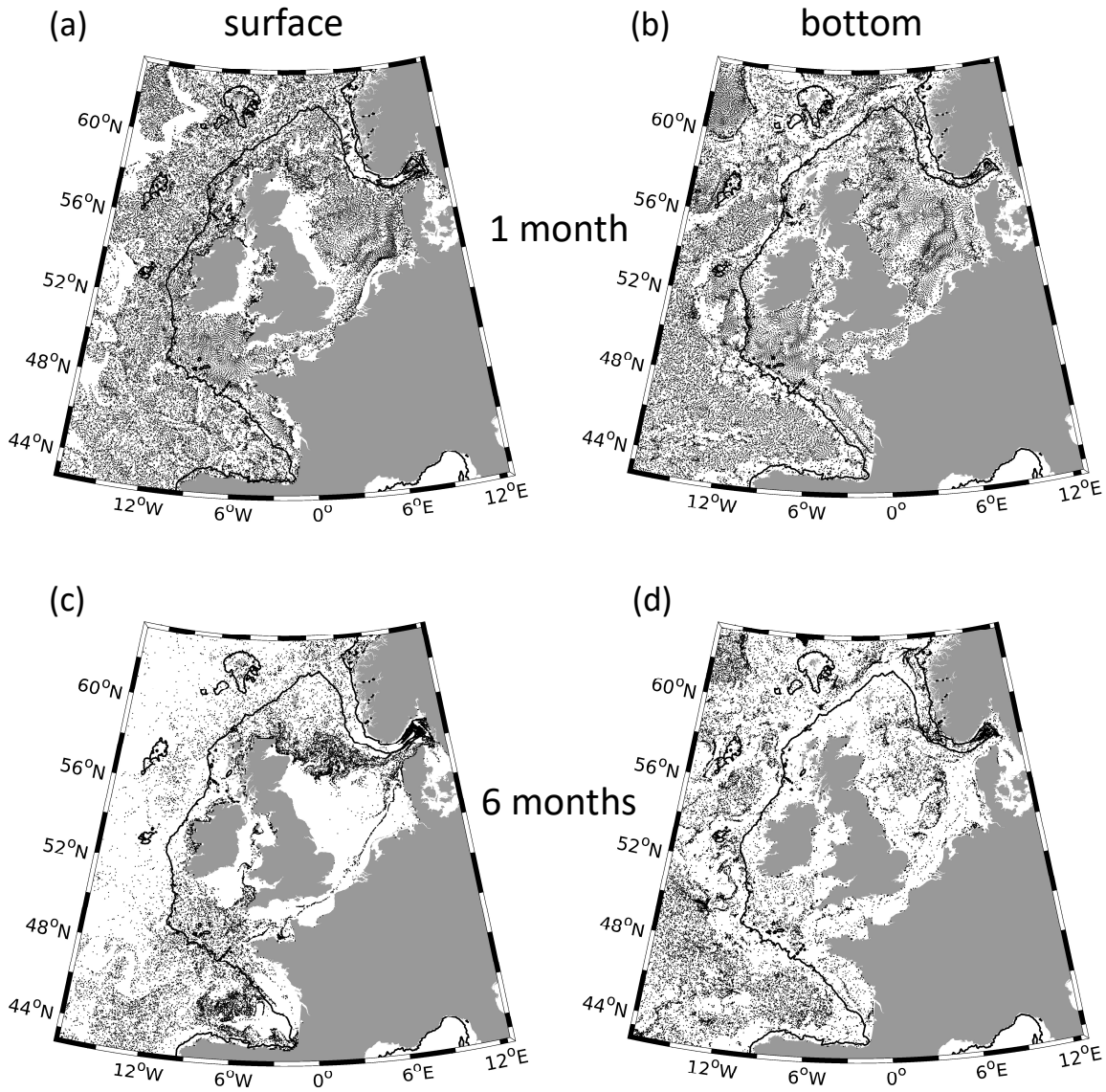
(a)
surface
(b)
bottom
1 month
(c)
(d)
6 months
60°N
56°N
52°N
48°N
44°N
12°W
6°W
0°
6°E
12°E

Fig. 4.

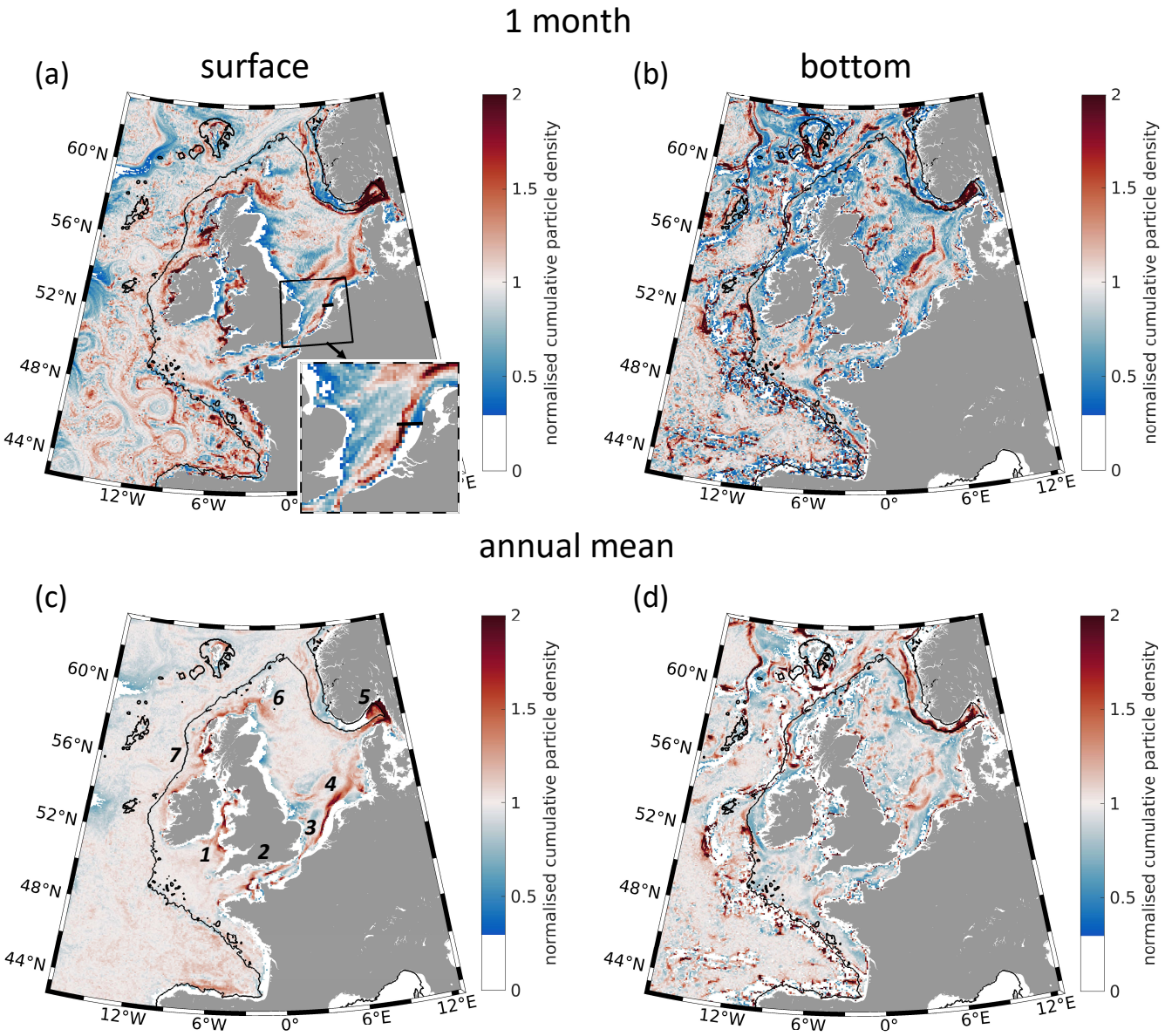
1 month
(a)
surface
(b)
bottom
annual mean
(c)
(d)
60°N
56°N
52°N
48°N
44°N
12°W
6°W
0°
6°E
12°E
normalised cumulative particle density
0
0.5
1
1.5
2
1
2
3
4
5
6
7

Fig. 5.

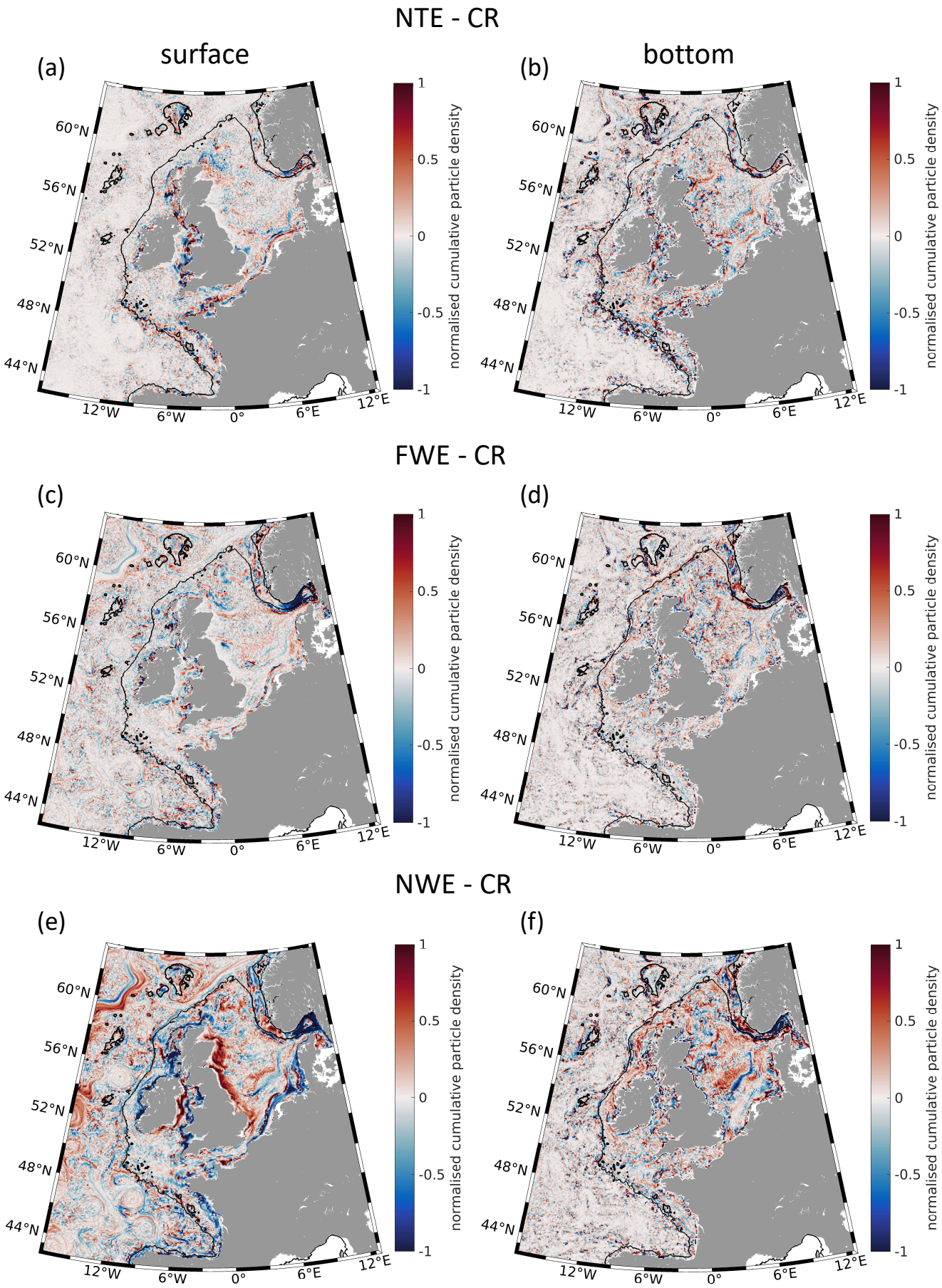
NTE - CR
surface
bottom
(a)
(b)
FWE - CR
(c)
(d)
NWE - CR
(e)
(f)
60°N
56°N
52°N
48°N
44°N
12°W
6°W
0°
6°E
12°E
1
0.5
0
-0.5
-1
normalised cumulative particle density

Fig. 6.

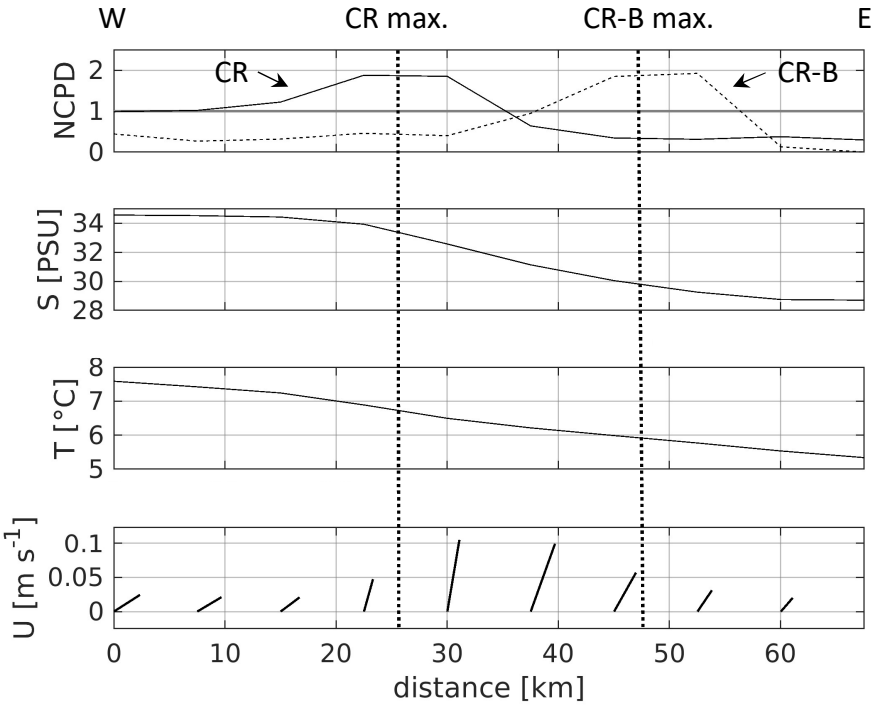

Fig. 7.

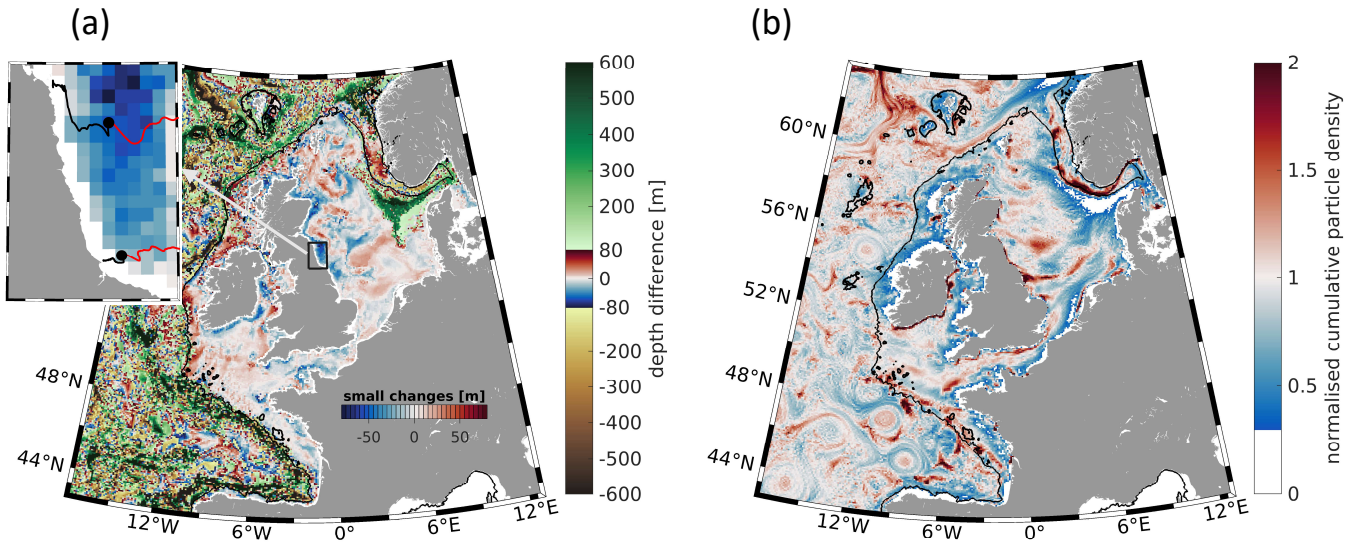
(a)
(b)
600
500
400
300
200
80
0
-80
-200
-300
-400
-500
-600
depth difference [m]
small changes [m]
-50
0
50
48°N
44°N
12°W
6°W
0°
6°E
12°E
60°N
56°N
52°N
2
1.5
1
0.5
0
normalised cumulative particle density

Fig. 8.

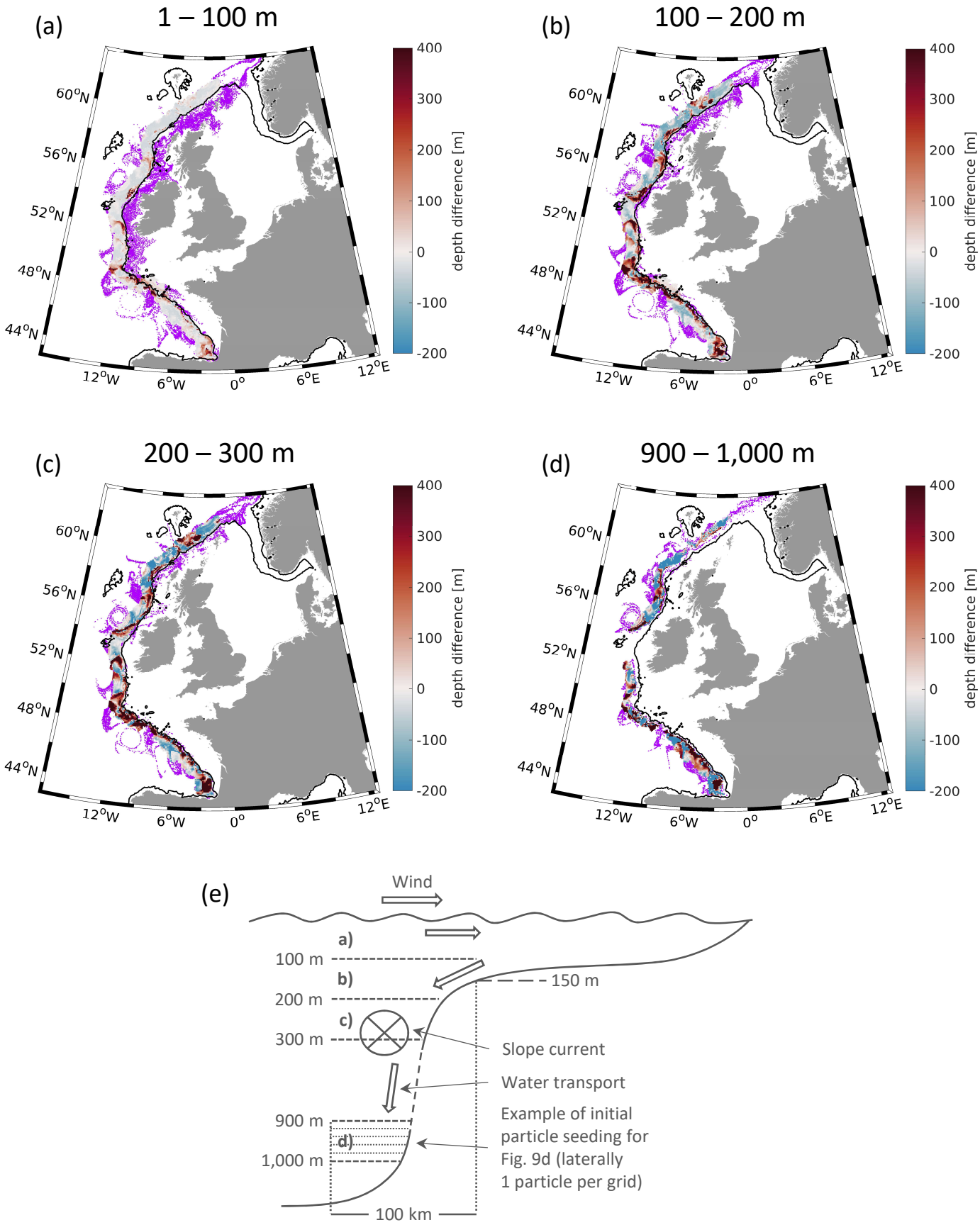
(a)
1 – 100 m
(b)
100 – 200 m
(c)
200 – 300 m
(d)
900 – 1,000 m
60°N
56°N
52°N
48°N
44°N
12°W
6°W
0°
6°E
12°E
400
300
200
100
0
-100
-200
depth difference [m]
(e)
Wind
a)
100 m
b)
200 m
c)
300 m
900 m
d)
1,000 m
150 m
Slope current
Water transport
Example of initial
particle seeding for
Fig. 9d (laterally
1 particle per grid)
100 km

Fig. 9.